Galactic Emission Mapping at 2.3 GHz

Arman Cingoz

Senior Honor Thesis

Department of Physics

University of California, Berkeley

Advisor:

Dr. George Smoot III

May 14, 2002

Contents

Abstract

The main topic of this thesis is the data analysis of Galactic Emission at 2.3 GHz. Data taken in Colombia (1995) and in Brazil (1999) is analyzed simultaneously. Several RFI removal and de-striping techniques are developed. System parameters such as the gain, system temperature, and the susceptibility of the gain to temperature are also deduced from the data due to the lack of experimental measurement of these quantities. Finally the maps are merged together into a final map covering $\sim$50% of the sky.

Acknowledgments

The work presented here is a result of a two semester collaboration with other students. Specifically, none of this would be possible without the hard work of James Lamb, Nishanth Rajan, and Kate Marvel. We were also fortunate enough to have Dr. Camilo Tello, Dr. Domingos Barbosa, and of course Dr. George Smoot as invaluable resources.

I would like to thank Camilo for helping me get started in data analysis which was completely a new territory for me. With his vast knowledge of GEM, both in hardware and software, he has guided us all the way through. In fact, initially, his Fortran code was used for time ordering and some of the shaft angle encoder calibrations which was slowly replaced by IDL code later on. Most importantly however, I would like to thank him for his patience and willingnes to listen to our ideas. He was never afraid to admit that there might be a better way.

I would like to thank Domingos for all of his help in the visual side of things. The final projections on to the sphere were created with his help using Healpix. I would also like to thank him for brightening may day with a smile or a joke, especially on the rides down the Hill at 6:50 p.m.

I have learned so much outside the classroom in the last two years due to my research experience. The person responsible for all I have learned is of course Dr. George Smoot. I would like to thank him for giving us the freedom to choose our own path. We have made many mistakes along the way; we have re-invented the wheel out of sheer ignorance so many times. But, he has been patient enough to let us find our own way to knowledge. I would also like to thank him for giving me the opportunity to go to Brazil. It was a real fun experience.

Finally, to the CMB ROPE thugs... I could not have done it without you. I would like to thank Jim for all of his hard work and determination, Nish for all the laughs and being the "Boss," Eric for his seemingly infinite knowledge, and Kate for putting up with me. I wish all of you the best of luck in the future. These last two years have been truly memorable... from sheet metal flying off the roof of building 50 to wrongful arrests at airports.

1 Introduction

A precise measurement and full sky maps of the diffuse Galactic emissions are really important in determining the dynamics of the Cosmic Rays and the galaxy overall. Synchrotron radiation from relativistic electrons accelerated through the Galactic magnetic field is the dominant source of emission at lower frequencies (up to few GHz). Free-free (thermal bremsstrahlung) emissions become the main component of the emissions at mid-frequencies ranging from 20 GHz to 60 GHz. At higher frequencies, the emission from the galactic dust becomes important. While the mechanisms of these emissions are well understood from a theoretical point of view, the parameters that govern their intensity spectrum have not been determined precisely. As a result, their absolute intensities and spatial distributions are not well known.

Moreover, the galactic emissions have become the limiting factor in cosmic microwave background (CMB) anisotropy measurements. Since most CMB measurements are made above 5 GHz, the contribution of the galactic emission is $\sim 10^{-3}$ K. However, the fluctuations of the galactic foreground is $\sim 10^{-6}$ K [1]. Therefore, although not a big source of contamination for measurements of the total intensity of CMB, the galactic emission is important in anisotropy measurements which are comparable to the galactic fluctuations. Since the Galactic foreground can not be eliminated using experimental techniques (even in satellite measurements), it is very important to understand the spatial and spectral variations of the foreground, especially in the frequency range dominated by the synchrotron and the free free emissions, to separate the foreground from CMB. Existing surveys can not provide the desired accuracy due to uncertainties in the baseline and gain ($\pm$ 3 K and 10% for Haslam *et al.* 1982 at 408 MHz and $\pm$ 0.5 K and 0.5% for Reich and Reich 1988 at 1420 MHz) and striping effects. Hence, accurate maps at several frequencies are needed to extrapolate the galactic emission to higher frequencies where most CMB measurements are made.

Galactic Emission Mapping project (GEM) is an international collaboration established to produce full sky maps at multiple frequencies ranging from 408 MHz to 10 GHz (De Amici *et al.* 1994; Smoot 1999). The collaboration was initially established by groups in Brazil (INPE/CNPq), Colombia (CIF and Observatorio Astronómico), Italy (CNR), and USA (Lawrence Berkeley National Laboratory/UCB). Initial 408 MHz [24] and 1465 MHz [22] maps have already been made from data taken in Owens Valley desert near Bishop in California, Viella de Leyva in Colombia, and Cachoeira

Paulista in Brazil. 2.3 GHz data was also taken in Colombia (1995) and Brazil (1999). The analysis of this data is the topic of this thesis.

2 Galactic Emission

As stated in the introduction, the three major sources of radiation in the galaxy are synchrotron radiation, free-free emissions, and the galactic dust. Figure 1 summarizes the frequency dependence of these emissions as well as CMB and CMB anisotropy. As it can be seen, the galactic dust is not an important factor at 2.3 GHz. Moreover, the free-free emissions do not play a major role far away from the galactic plane. Therefore, I will not talk about these emissions in detail. Synchrotron radiation, on the other hand, is the dominant source of radiation at 2.3 GHz. Most of the following information and equations are adapted from *Fluctuations in the Cosmic Microwave Background*, Banday, A. 1992 [1].

Galactic Dust

As the contribution from the synchrotron radiation falls considerably above 30 GHz, the galactic dust begins to dominate even at high latitudes. In the micrometer range of the spectrum, the dust emission is modeled as the blackbody temperature T_d modified by a frequency dependent emissivity $Q_\nu = K\nu^\alpha$. Once the frequency dependence of Q_ν is established, it is easy to derive the equilibrium temperature by balancing heating by photon absorption from the Interstellar Radiation Field (ISRF) and cooling by photon emission. The nature of the dust emission is quite complex, however, due to the structure and composition variations of the grain medium, variable dust/gas ratio and the variations in the ISRF.

Free-Free Emission

Free-free emissions are the thermal bremstrahlung radiation from the ionized gasses within in the galactic plane. Free electrons accelerated due to high temperatures at the galactic center radiate at a temperature

$$T = T_e(1 - e^\tau) \tag{1}$$

where T_e is the temperature of the gas and τ is the optical depth. This equation can be simplified for optically thin gasses (which is the case at 2.3 GHz) and be written

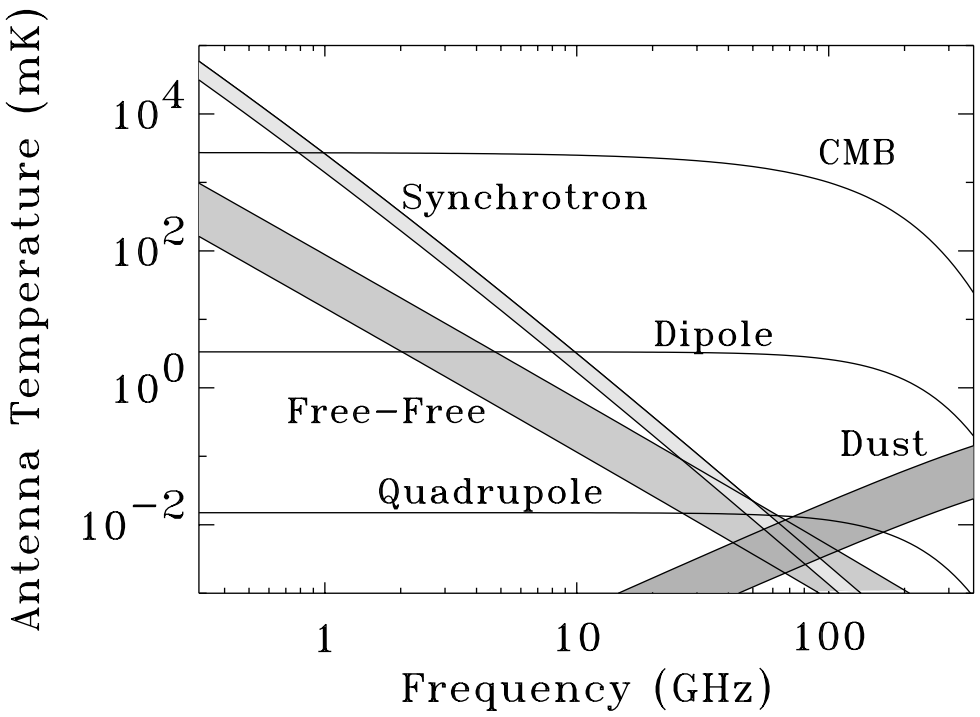

Figure 1: Frequency dependence of various galactic emission. The figure is reproduced from [20].

as

$$T = T_e \tau \tag{2}$$

where τ is given by:

$$\tau = 8.235\text{x}10^{-2} a(\nu, T_e) \left(\frac{T_e}{K}\right)^{-2.1} \left(\frac{\int n_e^2 ds}{pc\ cm^{-6}}\right) \tag{3}$$

The factor K=3.014 x 10^{-2} and $a(\nu, T_e)$ is a observational correction parameter [1]. As a result of the ν dependence of τ, the temperature of the free-free emission has a power law dependence. Since this emission is thermal, it is important at the plane of the galaxy and dominates above 2 GHz, but its contribution at higher latitudes are negligible.

Synchrotron Radiation

The synchrotron radiation is due to relativistic cosmic electrons losing energy in the magnetic field of the galaxy. Its large scale distribution can be described as a central disk on the plane of the galaxy surrounded by a weak radio halo. Its smaller scale

variations depend on various parameters. These parameters include the spatial and intensity variations of the galactic magnetic field, energy and spatial distribution of the electrons in the galaxy, and the variation of these parameters between the disk and the halo.

The energy spectrum of the electrons varies according to a power law since the synchrotron radiation intensity decreases with increasing frequency according to a power law. Therefore,

$$N(E)dE \sim E^{-\gamma}dE \tag{4}$$

where γ is the spectral component. This results in a brightness temperature of the form $T_b \propto \nu^{-\beta}$, $\beta = (\gamma + 3)/2$. The reason for this dependence is due to the volume emissivity defined as:

$$\epsilon(\tau) \propto B_{\perp}^{(\gamma+1)/2}\nu^{-(\gamma-1)/2}n_e(l) \tag{5}$$

where $B_\perp$ is the perpendicular component of the magnetic field along the line of sight, $n_e(l)$ is the density of electrons along the line of sight at a distance l. The intensity is given as the integral of the volume emissivity along the line of sight ($\int \epsilon(\nu)dl$). Finally, the brightness temperature is related to the intensity as follows:

$$T_b \propto I(\nu)/\nu^2 \propto \nu^{-\beta} \tag{6}$$

At energies corresponding to few GHz, the spectral index β is approximately 3. However, as the energy increases, the energy spectrum and hence the radiation spectrum steepens. Since the energy at which the spectrum steepens is dependent on the particular point in the galaxy (the spatial variations in the magnetic field coupled with the lifetime of the electrons), the spectral index must also be dependent on position as well as frequency.

Determination of the exact value of the spectral index at a frequency requires data not only at that frequency but also at another frequency. β can be determined from the data using the following formula:

$$\beta = \frac{\log T_1/T_2}{\log \nu_1/\nu_2} \tag{7}$$

This formula assumes that β does not vary between the two frequencies considered. This of course is not true but nevertheless, β can be viewed as the linear slope between the two frequencies.

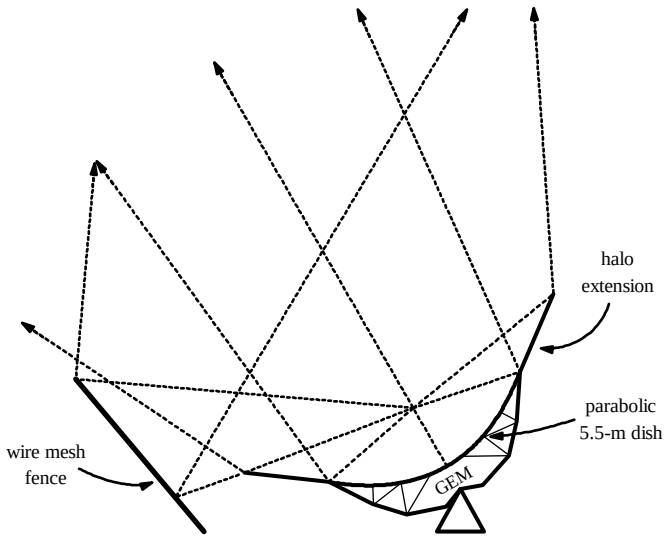

Figure 2: Diagram of the GEM dish, rim halo, and stationary ground shield. The figure is from [23].

3 Apparatus

In this section, I will talk about the radio telescope and the receiver used to make the measurements in Colombia and Brazil. Since I was not involved with the design or construction of any part of the apparatus, the information presented was gathered from various sources (see [22], [23], [24], [25]) as well as personal involvement in the partial design of the 5 GHz receiver.

3.1 Dish and Observational Technique

One of the biggest problems with making full sky maps is the relative calibration of data taken at different sites. Usually, these measurements are made with different telescopes varying in angular resolution and sensitivity. To avoid this problem, GEM utilizes a small, 'portable' dish which can be moved from sight to sight. As a result, all the data is taken with the same dish and receiver, simplifying data merging later on. GEM uses a 5.5 meter, parabolic Scientific Atlanta dish on an alt-azimuth base. The parabolic dish is made out of 12 petals which eases the transportation of the dish without any damage to the surface. The dish has a removable tripod extension to allow for both prime focus (such as 408 and 1450 MHz backfire helix antennas and 2.3 GHz receiver) and cassegrain feed (such as the planned 5 GHz and 10 GHz receivers).

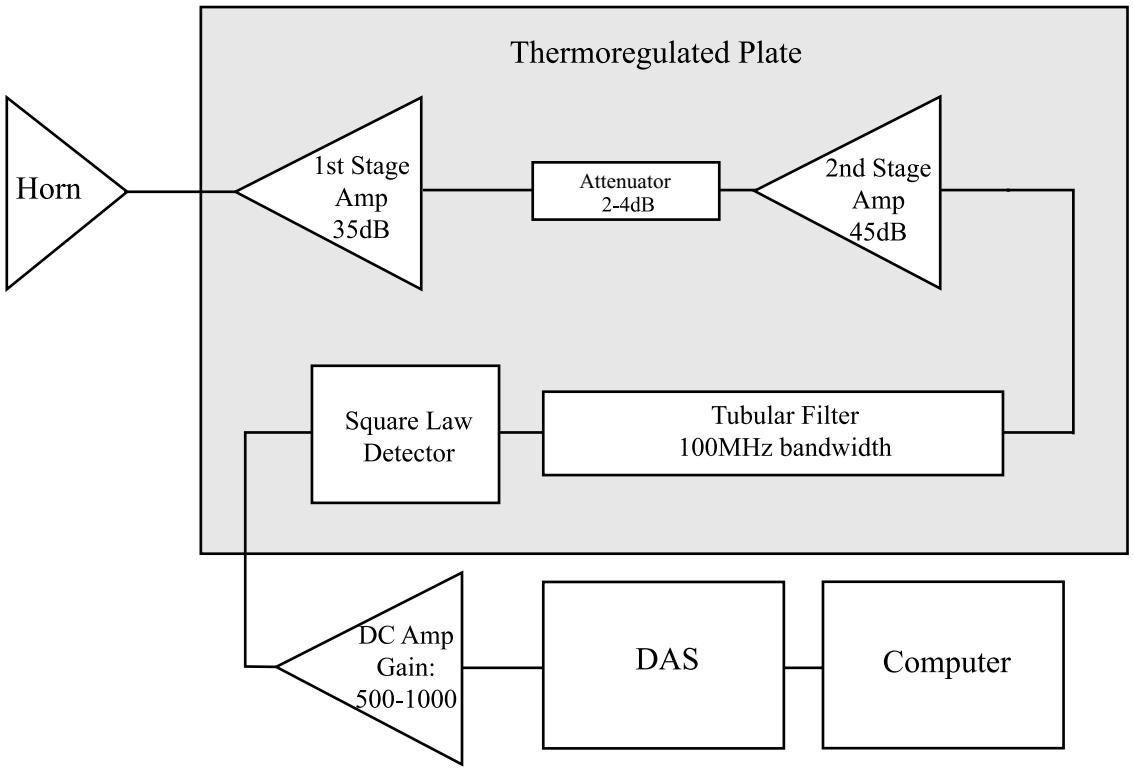

Figure 3: Schematic diagram of the receiver components.

The 2.3 GHz receiver is small and light enough to be attached to the tripod at the prime focus. However, due to the finite length of the reciever box, extensions were added to the tripod to raise the horn to the focal point. In fact, as I will discuss later, Colombia data suffers from incorrect positioning of the extensions and hence an out-of-focus horn.

Data is taken by tilting the dish 30° from the zenith and rotating it in azimuth at 1 rpm. As a result, a 60° wide declination band is covered as the Earth rotates throughout the day. In order to avoid ground contamination and the striping effects it leads to due to observational technique, a double shield configuration is used on the GEM dish. The first shield is a co-moving rim halo extending 2.1 meters from the dish petals, while the other is a 5 meter high wire mesh fence, inclined 50° from the halo extensions, surrounding the entire dish. An extensive study of the effects of the shielding is discussed in [23]. Although quite effective at lower frequencies, due to the size of the wire mesh, the fence is not adequate at 2.3 GHz (see figure 13a). Currently, a new fence is being constructed in Brazil for future observations at 2.3 GHz and higher frequencies.

3.2 Receiver

The information in this section is provided by Marco Bersanelli who designed and built the 2.3 GHz receiver. As stated in the last section, the receiver-horn assembly is quite compact and is mounted on the prime focus. The feed horn has a measured VSWR of 1.023 with a symmetric beam of 120° at -12 dB. To minimize noise due to coaxial cable between the horn and the first stage amplifier, the throat of the horn is enclosed within the receiver box.

The receiver is a total power radiometer. A short SMA coax cable connects the waveguide-coax transition to the first stage amplifier. The amplifier is a High Electron Mobility Transistor with a gain of about 35 dB and 30 K noise temperature at the operating temperature of 300 K (Berkshire Technologies S-2.3-30-RH). Its response is flat in the desired region of 2.25 to 2.35 GHz band. The output of the first stage amplifier is attenuated 2-4 dB in order to avoid saturation at the second stage amplifier input. The attenuated signal is then fed into the second stage amplifier (MITEQ AFS4-02200240-20-10P-4), which provides an additional 45 dB of gain. Then, the amplified signal is passed through a tubular pass band filter with a 100 MHz bandwidth (TRILITHIC 4BC2300/100-3-KL) centered around 2.3 GHz. The output of the filter is rectified using a square-law diode detector. The DC voltage is amplified by a factor of 500 or 1000 depending on the setting and then integrated for 0.56002 seconds.

The entire receiver is temperature controlled in several ways. The RF-chain is mounted on a temperature controlled aluminum plate. The temperature of the plate is measured by a thermister diode which feeds back to the temperature regulation electronics that control the current flowing into the power resistors that heat the plate. The aluminum plate is enclosed in a RF-tight box along with the throat of the feed horn, electronic thermometers, temperature regulation electronics, DC amplifier, and integrators. The box is insulated using thermal insulation foam and is cooled by a peltier device that regulates the ambient temperature of the box. However, the device is too small to maintain the temperature at normal operational level as the elevation of the sun becomes comparable to the elevation of the beam. The temperature within the box is monitored at the HEMT amplifier, the detector diode, the feed horn, and in the electronics box by AD590 transistors. To correct for baseline drifts due to temperature changes, a noise source firing is injected into the data stream every 80 seconds.

3.3 Data Acquisition System and Software

The analog DC signal, along with all the housekeeping signals, is converted to digital at the Data Acquisition System (DAS). The output of the DAS is passed through a slip-ring which consists of many fine conductive needle points rotating with the dish over stationary conductive rings. The signal from the DAS is connected to the needles, while the rings are connected to the computer. This provides a reliable way of transferring the signals without hindering the rotation of the dish. At the center of the slip-ring sits the shaft angle encoder (COPI CP850-12AN-360-F-V) which outputs a voltage from 0 to $\sim$ 10 V depending on the orientation (rotation by angle θ) of its shaft from an arbitrary reference position. This signal is also fed into the DAS.

The DAS samples all the signals and holds them for the duration of the integration time of the sky signal and then creates a frame consisting of a sync word to mark the beginning of each frame, the DAS frame number and all the signals. This TTL digital signal is converted into RS232 standard and sent to the serial port of the computer. The data is received and saved to disk by National Instrument LabView program. The LabView program converts hexidecimal words into integers which represent the digital steps. The DAS is adjusted to sample in a 20 V range from -10 V to 10 V. Since the Analog to Digital converter is 16 bits, there are 65535 steps where the 0th step corresponds to -10 V and the 65535th step corresponds to 10 V. Apart from these conversions, in order to keep track of the pointing of the telescope, the UT time for each frame or the first frame of each file is required. While there are no limitations on the file sizes in Colombia data (they are as long as the operator wishes to run the telescope), the Brazil datasets are automatically closed after 1.5 hours and a new file is started without any frame losses in between. This helps both on the transfer and data analysis phase while minimizing data loss during observation due to computer crashes or electrical problems.

4 Data Analysis

The entire data that was analyzed comes from two locations. Between June 1 and June 18, 1995, 159.3 hours of data was taken at 2.3 GHz in Villa de Levya ($\sim$ 180 km from Bogotá), Colombia. The latitude, longitude, and altitude of this site are 5° 37' 7.84" N, 73° 35' 0.53" W, and 2,173 m.a.s.l. respectively. An additional 542.9 hours of data was taken at Cachoiera Paulista ($\sim$ 150 km from San Jóse dos Campos),

Brazil between May 18 and June 17, November 11 and November 26, 1999. The latitude, longitude, altitude of this site are 22° 41' 0.74" S, 44° 59' 54.34" W, and 572.07 m.a.s.l. (all of the numbers given suffer from a systematic uncertainity of 100m allowed by the Department of Defense). The observations cover -24° 22' $< \delta <$ +35° 37' for Colombia and -52° 23' 14.1" $< \delta <$ +7° 8' 50.98" for Brazil.

Unfortunately, at both locations, the receiver was not calibrated. As a result, the actual gain, system temperature, and the susceptibility of gain to physical temperature were not determined during the observation stage. We were forced to calculate these parameters from the data using sun and moon crossings (see calibration section). However, this procedure resulted in large fractional errors in all of these parameters. Moreover, the procedure was not conclusive and useful in Colombia data due to the following reasons: The tripod extensions were missing which led to an out of focus feed horn; there were electrical problems in Colombia data that shift signal levels from positive to negative voltages (or vice versa). As a result, calculated parameters were in complete disagreement with Brazil data. Since these problems do not exist in Brazil data, Colombia data was calibrated using the overlap region between the two maps.

4.1 Data Analysis Pipeline Overview

In this section, I would like to give an overview of the entire data analysis process before going into the details of each step. These steps are summarized in figure 4.

Text Conversion The Colombia data was taken on a Macintosh computer, and as a result must be converted to PC ASCII format before analysis since we used IDL on a PC to process the data.

Digital steps to Voltage Conversion As discussed in the Apparatus section, the DAS outputs digital steps that need to be converted into physical voltages. In addition to this conversion, data is searched for sync losses (sudden loss of data frames for a random amount of time), and the time stamp of each frame is either fixed or created.

Shaft Angle Encoder Calibration There are couple of numbers that need to be computed to get the correct azimuth reading out of the encoder. First of all, the maximum voltage that the encoder outputs is theoretically 9.99758 V. However, in reality, this number differs from 9.99758 V and must be calculated in order

to convert voltages into angles correctly. The second problem is that there are incorrect encoder readings as the encoder voltage goes from maximum voltage to 0 V: an intermediate value is recorded between the maximum and the minimum which need to be replaced with the correct value. Finally, the reference of the shaft encoder is completely arbitrary. The difference between true South and this arbitrary reference value must be calculated for correct pointing. Also, although the elevation is approximately 60°, it must again be calculated precisely. Both the azimuth and the elevation calibration is achieved using the moon and the sun crossings. This also requires accurate ephemeris generation for the moon and the sun

After the pointing is established there are two different paths that can be taken. Either system parameters are determined or a map must be made (data binned by right ascension and declination rather than time order) in order to develop techniques to deal with radio frequency interference (RFI) or sidelobe contamination. We chose to pursue the later route first since any noise due to RFI or contamination would result in incorrect calculations for the receiver parameters.

Mapping and RFI Removal

Mapping In order to make preliminary maps, we use the results of the initial calculations presented in the internal paper by Torres [25]. However, since these parameters are inaccurate, it is necessary to deal with the drifts in the baseline. Finally, the noise source firings are extracted and the data is binned by right ascension and declination.

RFI removal Outliers within each pixel are determined and removed from the map.

Ground contamination The Brazil data has severe striping in the Northern part of the map due to sidelobe pickup from the ground. This problem is partially dealt with using an iterative method suggested by Prof. Smoot.

Receiver Calibration To determine the system parameters, the beam pattern of the telescope is needed. This is yet again achieved using the moon and the sun crossing: The data is binned by the angles between the beam and the source object (moon or sun). The gain is calculated from the peak of the beam pattern, while the system temperature is determined using the moon as a hot

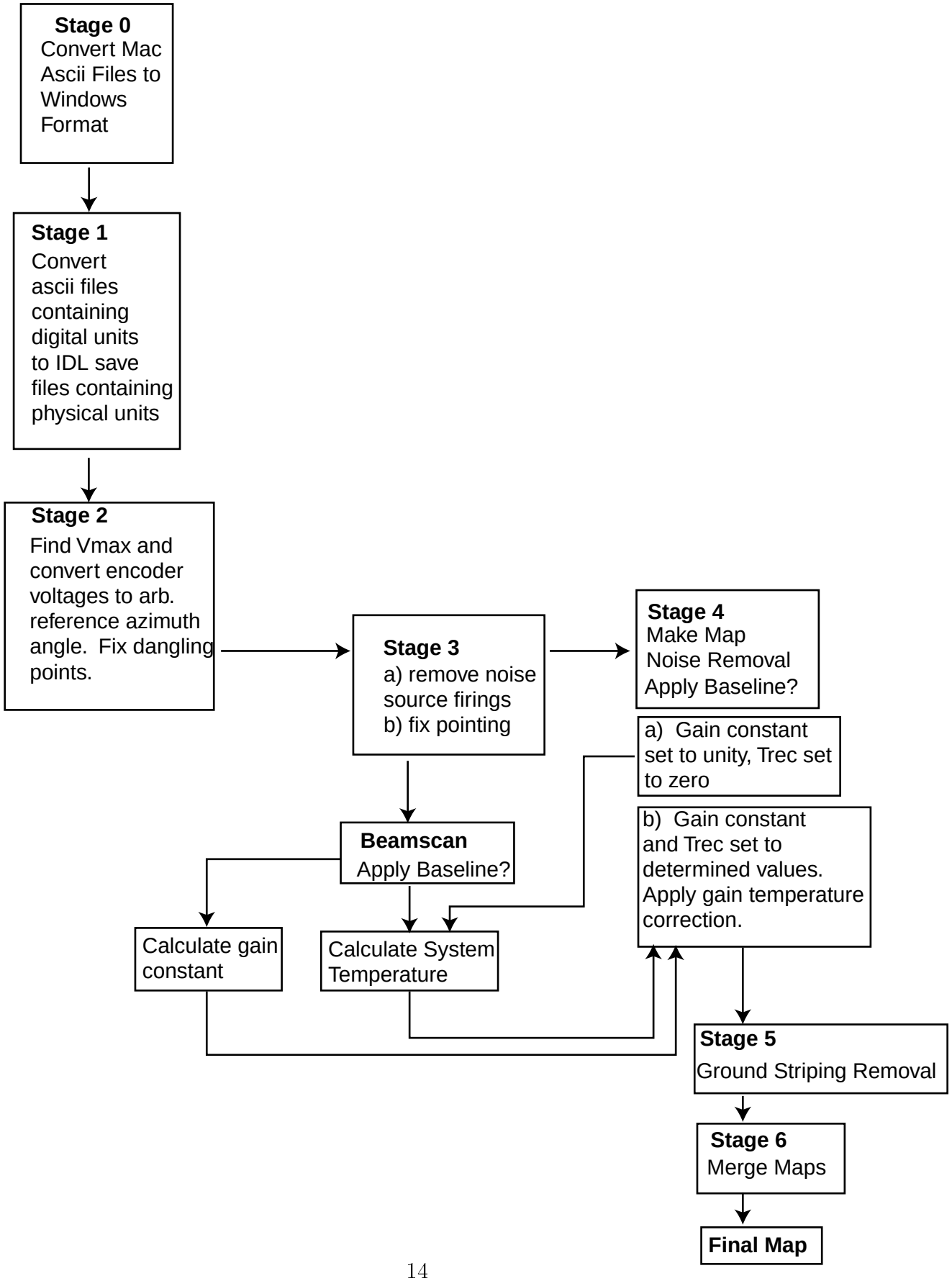

Figure 4: Pipeline Overview

source and a cold region of the sky. The susceptibility of the gain the physical temperature is determined by correlating the physical HEMT temperature with sky temperature.

Map Merging Once the system parameters are known, the final Brazil map is produced. The Colombia map is calibrated using the overlap region between the maps. Finally, the two maps are merged together.

4.2 Time Ordering

In this section, I will describe the procedure to put data in time order. The procedure is different for Brazil and Colombia data since different LabView and EPROM programs were used to save data to file.

Brazil Data

In Brazil, the EPROM was programmed to write frames in the following order: frame, elevation, signal, blank, T_{DIODE}, T_{HEMT}, T_{FEED}, T_{EL}, heater voltage, blank, blank, T_{NS}, noise source voltage, and azimuth. Each file is 16500 frames (approximately 1 hour and 34 minutes) long. At the end of each file, LabView opens a new file and continues to take data until the observer terminates the run. The time stamping for the files are determined using a GPS. Every time a new file is started, the UT time from the GPS is combined with the date to create a filename that is of the form YY_MM_DDhhmmssdd (year, month, day, hour, minute, second, decisecond). Therefore, the time stamp of the first frame of each file is stored as the filename. There are problems with this method, however, due to LabView crashes. Some of the files have names that do not conform to the above-mentioned convention. All of these files, as well as some that do have proper names, have a sync loss at the 99th frame for an indeterminate amount of time. Camilo Tello, who took the data in Brazil, has mentioned that this is due to LabView freezing for a while and then recovering to continue taking data.

Since this problem was also present during 1450 MHz measurement, a systematic way of dealing with these problems was already established. The procedure is as follows. For files with unconventional names, we check if the first frame of the file (using the frame number of the DAS) is contiguous to the last frame of the file closed right before the corrupt file. If it is, the time-stamp of the last frame of the previous

file is calculated from the filename of that file and 0.56002 seconds is added to it to calculate the time-stamp of the corrupt file. If for some reason, there is a sync loss between the two files, we check if the last frame of the corrupt file is contiguous to the first frame of the next file. If it is, 0.56002*the number of frames in the corrupt file are subtracted from the filename of the next file and assigned to the corrupt file. If there are sync losses within the file, almost always at the 99th frame, the frames before the sync loss are discarded to keep the frame numbers contiguous throughout the file.

Once all the files are corrected, file lists are formed that contain the name of files that were taken in one continous run (i.e. the DAS was never turned off in between these files). Using the filelists and the time-stamp of the filenames, each frame is assigned a Universal Greenwich Time (UT) by advancing the first frame time stamp by 0.56002 seconds * the frame number difference between the first frame and the current frame. Originally, we wrapped time around. Therefore, if a file contained two consecutive days, the UT would be reset to 0 at the beginng of the new day. However, further down the pipeline, we realized that it was much easier to deal with astronomical routines if we let the UT get larger than 86400 (24 hours in seconds). The reason for this was due to the sync losses. In files which start really close to 12 a.m. at night, the filename date stamp reflects the day in which the file started; however, due to sync loss problems the first frame might have a UT early in the morning next day. If the UT is wrapped so that it is less than 86400, astronomical programs execute under the assumption that frame was recorded in the morning of the first day which is obviously incorrect. However, if UT is not wrapped, it is larger than 86400 and is interpreted correctly as being in the next day.

Once the time-stamping is corrected, all the channels are converted from digital steps to voltages using the formula:

$$V = 10(\frac{du}{2^{15}} - 1) \tag{8}$$

where du is the digital step number. This formula is rather intuitive since for 0 du=-10 V, for 2^{15} du=0 V, and 2^{16} du=10V. In addition to voltage conversion, the temperature sensor voltages are converted to Celsius by a simple multiplication of 10. Finally, the data is saved in native IDL format in the following order: frame, time, elevation, signal, azimuth, T_{DIODE}, T_{HEMT}, T_{FEED}, T_{EL}, heater voltage, T_{NS}, and noise source voltage.

Colombia Data

The EPROM for Colombia is programmed to write frames in the following order: frame, time, elevation, signal, azimtuh, T_{DIODE}, T_{HEMT}, T_{FEED}, T_{EL}, heater voltage, blank, blank, T_{NS}, and the noise source voltage. The LabView program, however, is not set up to close and open data sets seamlessly. Therefore, there are gaps between each file as the operator manually closes and opens new files. The time stamping should be easier since every frame is time-stamped with a UT when it is written to file. However, a closer inspection shows that although these time-stamps have precision up to decisecond level, there are many contiguous frames that have the same UT time. The reason for this is that the WWV system used in Colombia cannot transmit more than once a second. Since the frame length is half a second, this limitation results in inaccurate time-stamping. Moreover, the sync losses in Colombia data are much more random and occur multiple times within a file. Frames adjacent to synclosses are corrupted as well and do not represent digital steps. As a result, they have to be removed from the datasets. The frames are properly time-stamped using the time-stamp of the first frame and recreating the time stamp of every frame afterwards by incrementing the time-stamp by steps of 0.56002 seconds. After these corrections, the signals are converted into real voltages, temperature readings are converted into Celsius, and the data is saved following the same conversions as the Brazil data.

4.3 Shaft Angle Encoder Calibration

4.3.1 Maximum Encoder Voltage

The shaft encoder used is a 12 bit encoder and hence has 4096 steps ranging from 0 V to 9.99758 V (theoretical). However, we do expect a small correction to this value due to variations in the manufacturing process. The process that deals with this problem does have an underlying assumption that the encoder is capable of recording 0 V. This assumption seems reasonable since it is relatively simple to produce this voltage reliably and testing with actual shaft encoders reveal that 0 V is achieved (testing done by James Lamb and myself in Brazil on two shaft encoders identical to the one used during the observations).

Once we make this assumption, it seems that it is rather straight forward to calculate the maximum voltage. Since for every rotation, the voltage decreases monoton-

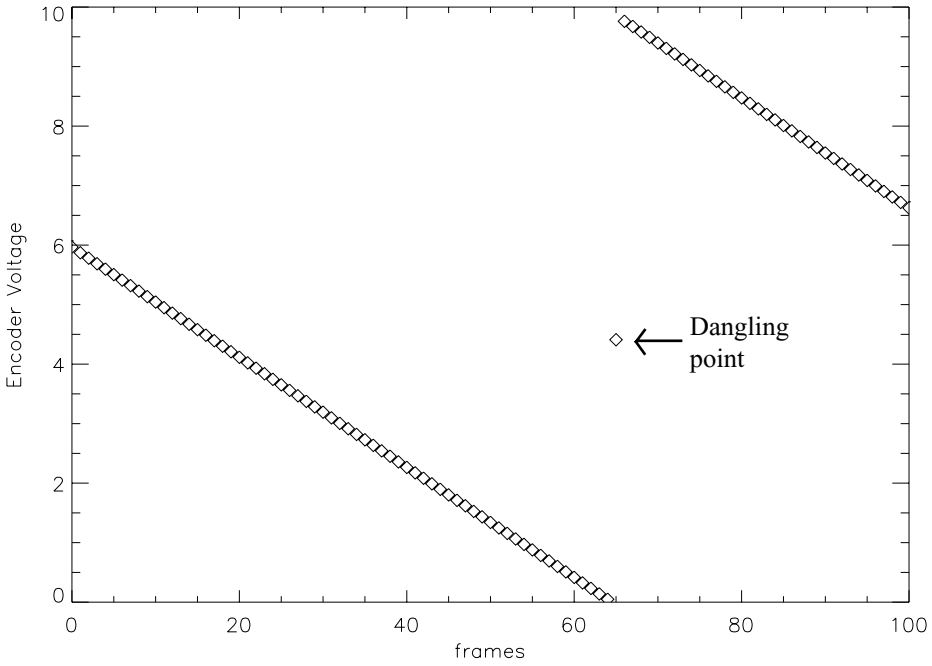

Figure 5: Encoder voltage transition from one rotation to the next. The voltage at the dangling point cannot be a real value since that would suggest the dish has rotated 180° in one frame.

ically from maximum voltage to 0 V (it decreases because GEM rotates counterclockwise) at a constant rate (the rotation period is consant at 1 rpm) until it suddenly jumps from 0 V to the maximum voltage, the average volts per frame (vpf) can be calculated from the monotonically decreasing sections. Then, using the assumption that the encoder is capable of outputting 0 V, we can calculate the difference between the minimum voltage recorded for the rotation and 0 V. If this is less than vpf, then the encoder must go through this difference before the sampled maximum voltage of the next rotation. As a result, the maximum voltage (V_{max}) of the next rotation should be:

$$V_{max} = V_{max_s} + (vpf - V_{min_s}) \tag{9}$$

where V_{max_s} is the sampled maximum voltage of rotation i+1, and V_{min_s} is the sampled minimum voltage of rotation i. However, there is a complication that requires a modification to the formula. Due to either manufacturing flaws, or lengthy cables between the encoder and the DAS (capacitance leading to exponential decay), the encoder response from 0 V to the maximum voltage is not fast enough. As a result, an intermediate voltage is recorded for one or two frames (dangling frames) before

the voltage jumps to the observed maximum (see figure 5). So, to calculate the V_{max}, equation 9 must be modified as follows:

$$V_{max} = V_{max_s} + (d * vpf - V_{min_s}) \tag{10}$$

where d denotes the number of dangling frames. This V_{max} does not correspond to exactly what is needed to convert voltages into angles. It must be corrected as follows:

$$V_{max} = V_{max}(1 - 1/4096) \tag{11}$$

This is analogous to the theoretical case where the maximum voltage of the encoder is not 10 V but 9.99758 (10-10/4096). Once the correct V_{max} is calculated, the dangling frame encoder voltages can be replaced with their correct values by propagating a nearby "good" frame voltage using vpf and the number of frames between the "good" and the dangling frame.

When equations 10 and 11 were used to calculate the V_{max} for the entire data, the results were a little startling. This intermediate result is shown in figure 6a. The sudden drops in the V_{max} value seem unphysical and a failure of the method used to calculate the parameter. To investigate further, an artificial test data was created which had a known maximum voltage. It was created by sampling a triangle wave in a way to deliberately avoid sampling the real maximum voltage. Some random noise was also inserted to give the artificial data a more physical structure. Figure 6b shows the results of the above formula on the artificial data. Clearly, the formula must be modified to correct the problem. A closer look at the sampled data revealed the problem. Equations 10 and 11 work for rotations where the sampled maximum voltage is a real maximum voltage (on the monotonically decreasing section); however, V_{max} is calculated incorrectly when the sampled maximum voltage is a dangling frame (see figure 7). This problem can be avoided by extending the calculation to adjacent frames as follows:

$$V_{max} = (Ang[k+1] - Ang[i-1] + [k - i + 2] * vpf)(1 - 1/4096) \tag{12}$$

where i is the index of the sampled minimum encoder voltage; k is the index of the sampled maximum encoder voltage; and Ang[i] is the encoder voltage at the ith index. The results of the implementation of 12 is shown in figure 8a and b for both real and artificial data. The calculated values for the shaft encoder maximum voltage were 9.900716 $\pm$ 0.01 for Brazil and 10.0066 $\pm$ 0.004 for Colombia. The difference is not

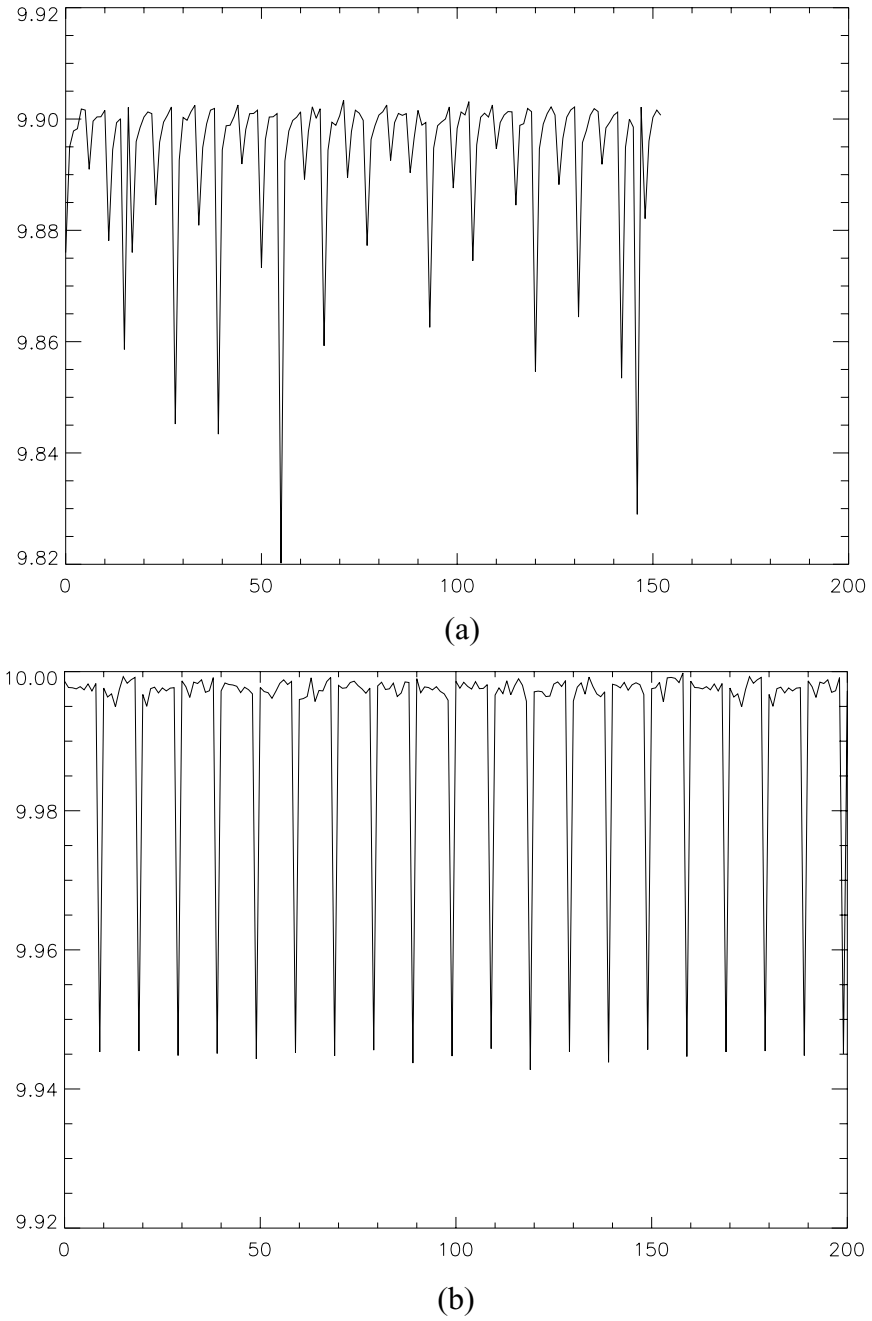

Figure 6: (a) V_{max} calculation for $\sim$ 150 rotations of real data with equation 10. (b) Same equation used on artificial data.

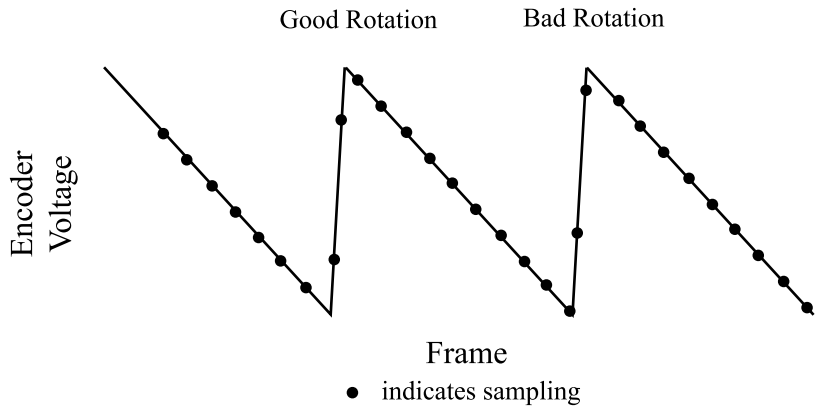

Figure 7: A schematic diagram of the encoder voltage. Equation 10 fails on "bad rotations."

too large; however, it is important to calculate V_{max} as accurately as possible since the absolute error on the conversion is not constant for all voltages and gets worse as the voltage approaches the maximum voltage.

4.3.2 Azimuth Offset and Elevation Correction

Once V_{max} is calculated and all dangling encoder voltages have been replaced with correct azimuth angles, the azimuth offset and the elevation correction must be calculated to complete the shaft encoder calibration. Since the encoder has an arbitrary reference 0°, an offset must be added to correct the pointing of the dish. In order to carry out this calculation, an identifiable source in the time ordered data-stream with known elevation and azimuth angles are needed. The best candidates for this source are the two brightest objects in the sky, the sun and the moon.

In time ordered data, the sun and the moon signals are gaussian shaped in each rotation with increasing amplitudes as the elevation of the source crosses the constant ∼60° elevation of the GEM beam. Figure 9 is a plot of the time ordered data during a moon crossing. The azimuth offset is determined by fitting least-square gaussians to the peaks in the rotations. The idea is to record the azimuth and the UT time of the gaussian peak and to compare it to the azimuth of the object (sun or moon) at the same UT. In practice, however, the azimuth of the peak falls in between two adjacent frames. As a result, the UT of the peak must be interpolated from the UT of the two frames. Since the time difference between the two frames is about half a second, a linear interpolation is sufficient:

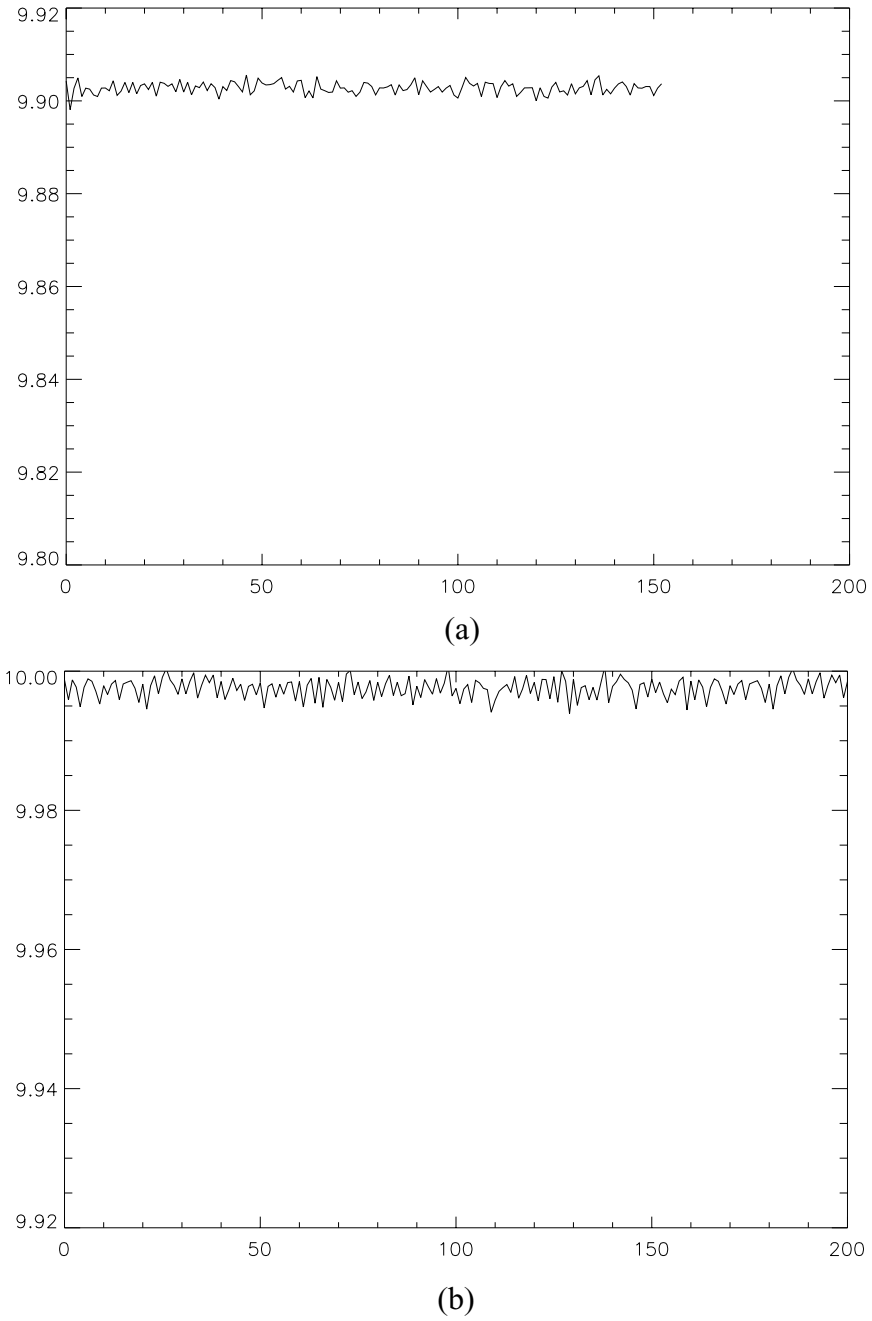

Figure 8: (a) Correct V_{max} calculation for the same rotations as in figure 5a. (b) Artificial data with the correct equation.

$$UT_{peak} = \left(\frac{Azi_{peak} - Azi_{min}}{Azi_{max} - Azi_{min}}\right)(UT_{max} - UT_{min}) + UT_{min} \tag{13}$$

where the min and max subscripts refer to the two frames. A similar interpolation must be made to find the azimuth of the object since the ephemeris data for the sun and the moon is generated for each frame. Since, the calculated UT is most likely to be in between the UT of two adjacent frames, the azimuth is calculated by:

$$EAzi_{obj} = \left(\frac{UT_{peak} - UT_{min}}{UT_{max} - UT_{min}}\right)(EAzi_{max} - EAzi_{min}) + EAzi_{min} \tag{14}$$

where EAzi refers to the ephemeris azimuth. This procedure was used for the moon in Brazil data since in the May-June observations, the azimuth of the sun is too close to the RFI beacon, which I will discuss later. The November data was not available at the time. Later on, the sun in the November data was used to double check the azimuth offset. Since there are no beacons in the Colombia data, the sun was used for the offset. The results are $242.36^\circ \pm 0.238^\circ$ for Brazil and $131.137^\circ \pm 0.131^\circ$ for Colombia.

Accurate and reliable ephemeris generation was a problem for this part of the data analysis. Initially, Fortran code written by Camilo Tello was used to generate the ephemeris. However, comparisons with Jet Propulsion Laboratory (JPL) Horizons website revealed small inconsistencies. The IDL Astronomical Goddard Library functions were also tested against JPL ephemeris. Goddard sun ephemeris was found to be in agreement with the JPL site with differences on the order of 10^{-3} degrees. The moon ephemeris, however, was still problematic. To alleviate this problem, we began to look for a way of generating JPL ephemeris. It is freely available from the JPL website along with IDL programs to convert datasets in Chebyshev coefficients (to save memory) into real ephemeris. However, none of the programs were able to generate ephemeris in topocentric coordinate system. Finally, a driver program written by James Lamb for Paul Heafner's code [9] was used to generate ephemeris accurate to 1 part in 10000 in comparison to JPL Horizon's website. This ephemeris was used to check the azimuth offset calculated using Tello's ephemeris. Due to uncertainties in the gaussian fits to the peaks, however, the error in the correction was greater than the correction itself (Heafner's ephemeris suggests that the azimuth correction is off by 0.019° but has a statistical error of 0.238°). Hence, the original azimuth offset was used.

The procedure for the elevation correction is similar to the azimuth offset. As stated above, as the object rises in elevation, the amplitude of its gaussian peak in

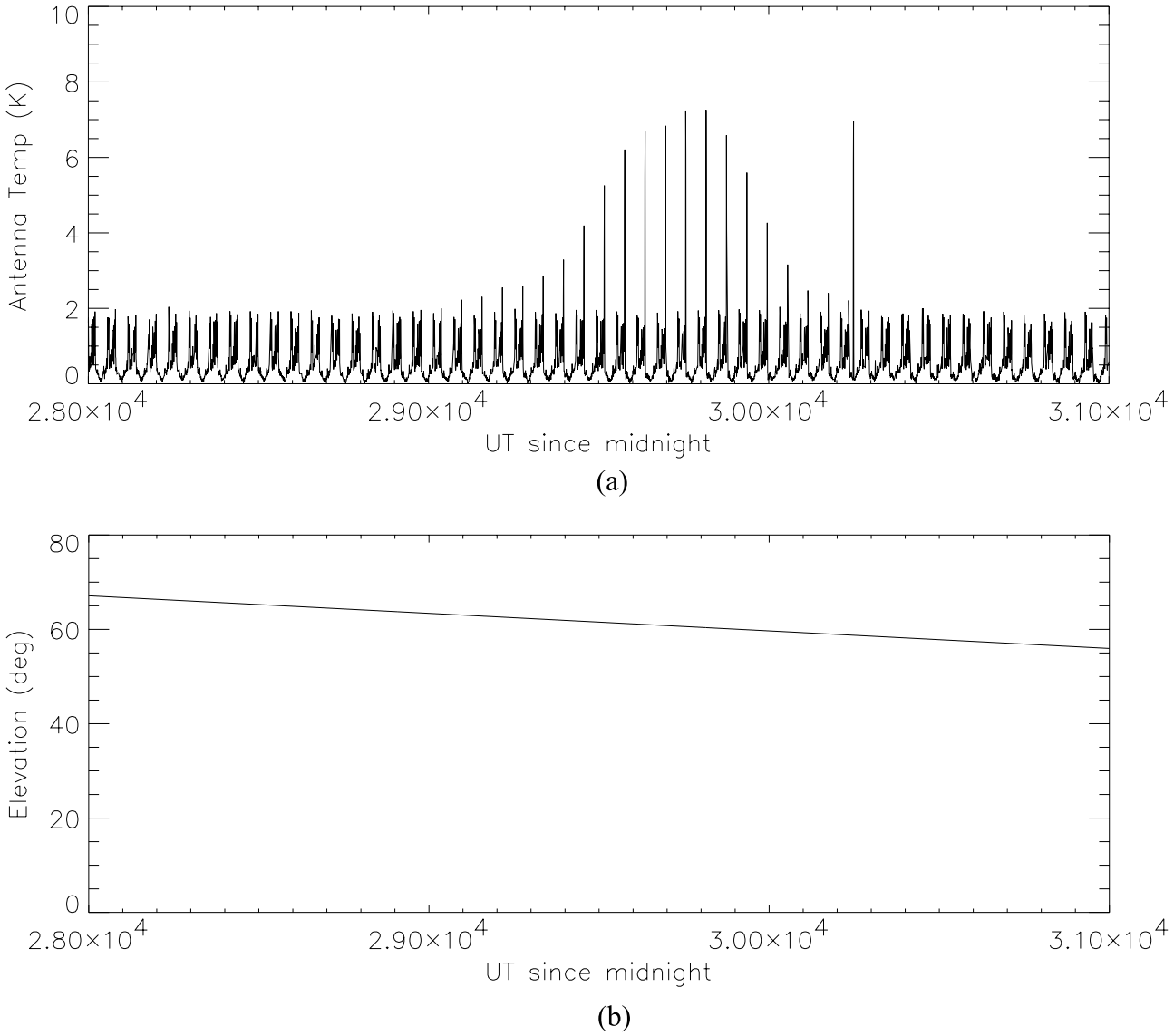

Figure 9: (a) Time ordered data during moon crossing. (b) The elevation of the moon at the same time.

each rotation rises until the elevation of the object matches the elevation of the beam and then decreases as the object continues to rise. To calculate where the object elevation intercepts the beam elevation, a gaussian is fitted to all of the object peaks in the data-stream. The results of this procedure was $60.1^\circ \pm 0.188^\circ$ for Brazil and $59.68^\circ \pm 0.06^\circ$ for Colombia data.

4.4 Mapping and RFI Removal

Once the pointing of the dish is established, the data must be analyzed further in time order before it can be binned in right ascension and declination.

4.4.1 Noise Source Removal

As described in the apparatus section, the signal is injected with a noise source every 80 frames for 4 frames to aid in the calibration of the baseline. Since the frames with the noise source firings are dominated by this signal, they must be removed before the map can be made. The noise source firings are removed using the voltage of the noise source by removing the frames when the voltage is above 1 V. A closer inspection reveals that there is a probability of the noise source firings bleeding into the frames adjacent to the 4 frames. As a result, 6 frames are removed. Ideally, noise source firings should be saved in a different file to be used later on. However, in the case of both Brazil and Colombia data, the noise source amplitude tends to oscillate with no correlation with the oscillations in the baseline. As a result, they are not a reliable source for calibration and have been discarded.

4.4.2 Baseline Correction

Since, initially, the system parameters are undetermined, an artificial baseline correction must be applied in order to eliminate baseline drifts due to physical temperature changes. The basic idea, adopted from Camilo Tello [23], is to find the minimum temperature of every rotation and to set it equal to a predetermined temperature. The assumption is that every rotation scans through a region in the sky away from the galactic plane. Although this is certainly true, treating the minimum sky temperature across the whole sky as a constant leads to an unnatural flattening of the baseline. However, at this stage it is perfectly reasonable to implement this method for preliminary maps.

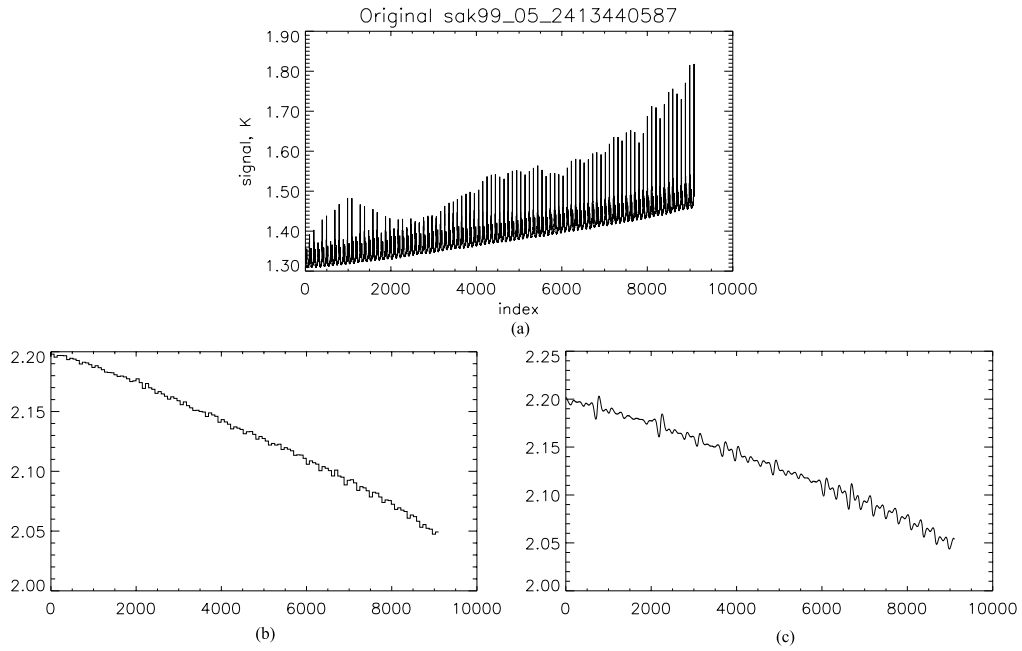

Figure 10: (a) Time ordered data with baseline drift. (b) 0th order baseline offset. (c) First attempt at fitting a cubic spline to the offset resulted in over-oscillations.

Camilo Tello's original method was to fit a 0th order polynomial fit to the fluctuations in the baseline and then subtract this drift to flatten the time ordered data. As a result, a constant value, which changes from rotation to rotation, is subtracted from the entire rotation. This leads to a baseline correction made up of many steps (see figure 10b). Although very simple to implement, this method introduces high frequency noise into the data due to the discontinuities in the baseline. This idea was taken a step further and implemented with a cubic spline interpolation which varies from one minimum to the next smoothly.

The cubic spline method is much harder to implement due to oscillations that may arise. Figure 10c shows the first attempt at implementing cubic splines and the resultant oscillations. These oscillations are a result of the irregular spacing in between the rotation minima. Several different methods are used to deal with this problem.

In Brazil data, this problem is systematic due to the geographical profile of the site. Since most of the mountains in Cachoeira Paulista are to the North, the minima of the rotations are concentrated toward the South. Since GEM uses 0° azimuth to be South, the minima of the rotations are either toward the beginning or the end

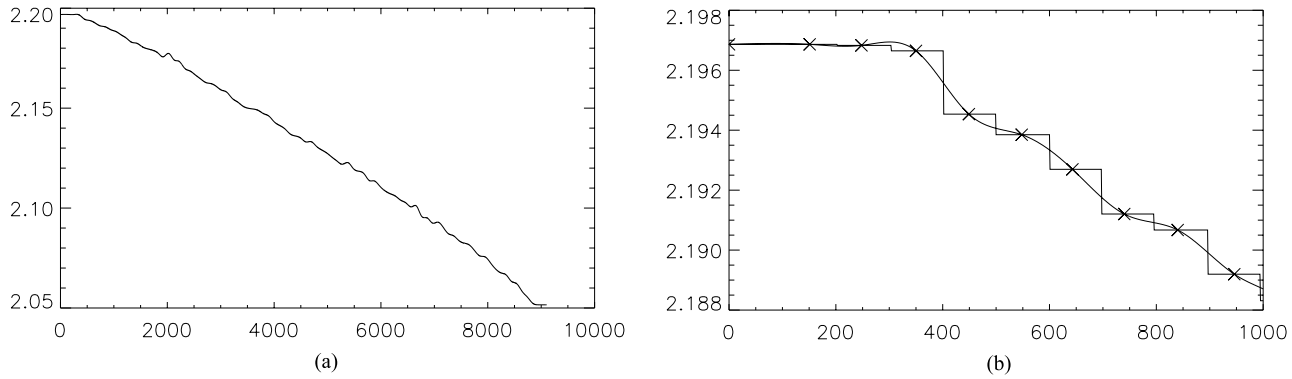

Figure 11: (a) The same baseline offset as in figure 10c with bins 180° out of phase with rotation. (b) A comparison of 0th order and 3rd order interpolation of the baseline (x indicate actual bin minima).

of each rotation (close to 0° or 360° azimuth). When adjacent rotations have their minima toward the end and the beginning respectively, oscillations are observed in the baseline. The easiest and most effective way of dealing with this problem is to shift the binning criterion 180° out of phase with the rotation. As a result, a minimum is searched for from the middle of one rotation to the middle of the next rotation (from 180° to 180°). In this binning scheme, the minima end up at the middle of the bin (at ~ 0 or 360^0) rather than at the edges, leading to a regular spacing between the minima (see figure 11a for an improved version of 10c).

In Colombia, unfortunately, there is no systematic reason for the irregular spacing. As a result, the clever binning scheme utilized for Brazil is not effective. The oscillations are avoided by checking if two minima indices are closer than 50 (which makes sense since there are approximately 100 frames in a rotation after noise source removal). If this condition is satisfied, then one of the indices is thrown out of the spline interpolation depending on which index maximizes the distance between itself and its remaining neighbors. As a result, the smoothest possible spline that fits the data best is achieved. There are, however, other problems that need to be dealt with. In some of the rotations, the minimum that is found is right next to a noise source removal. This makes the determination of the minimum unreliable since the signal could have been smaller in any of the 6 frames that were removed. Since this could lead to incorrect baseline for the rotation and affect the curvature of the spline, we decided not to include these points in the interpolation and let the spline vary smoothly from the previous rotation to the next one. Another problem that is characteristic of

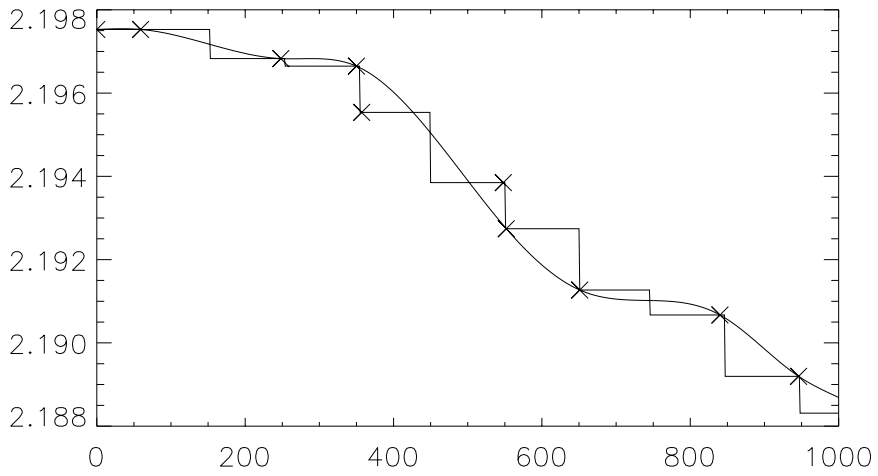

Figure 12: Over-oscillations in the case of too-close minima are avoided by ignoring one of the minima. The minimum that maximizes the distance between itself and its neighbors is kept.

the Colombia data is due to the electrical problems of the system. Some of the data includes negative voltage spikes which cause problems because they are calculated to be the minimum of the rotation and lead to a huge ripple in the baseline. They are dealt with simply by requiring the minimum voltage to be a positive quantity which only works for files where the data is positive with negative spikes. For files where the entire signal is negative, the signal is first shifted up to positive and then processed.

4.4.3 Mapping

Once the baseline is corrected, the signal must be converted from volts to Kelvin. The initial values for gain, system temperature, and the susceptibility of the gain to temperature were calculated by Sergio Torres [25] . The constant component of the gain, G_o is modified by the susceptibility as:

$$G = G_o/(1 + \frac{G_o * m * \Delta T}{T_{sys}}) \tag{15}$$

where m is the susceptibility and ΔT is the deviations from the mean temperature G_o and T_{sys} were calculated at. The signal in volts is multiplied by G, and T_{sys} is subtracted from it to give the signal in Kelvin.

After the conversion process, the signal is binned by right ascension and declination. During the binning process, the sun and the moon are removed from the data by rejecting any data where the sun is closer than 25° and the moon is closer than

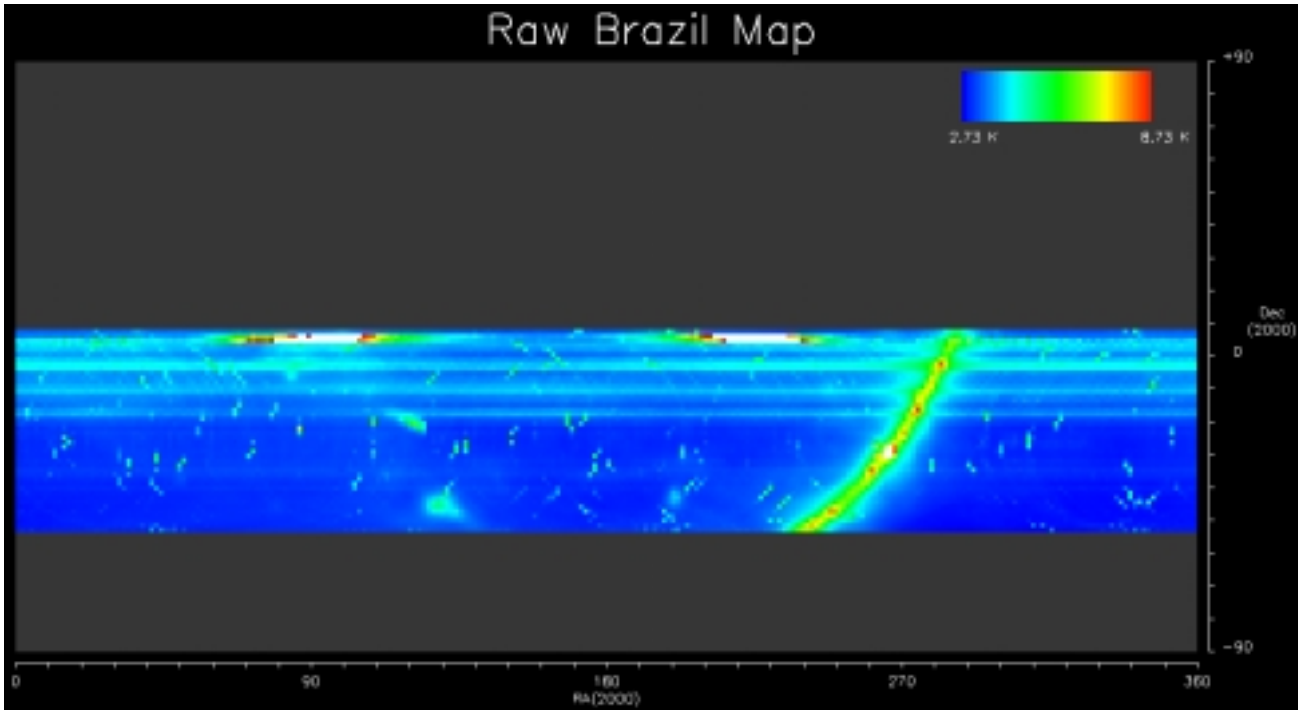

(a)

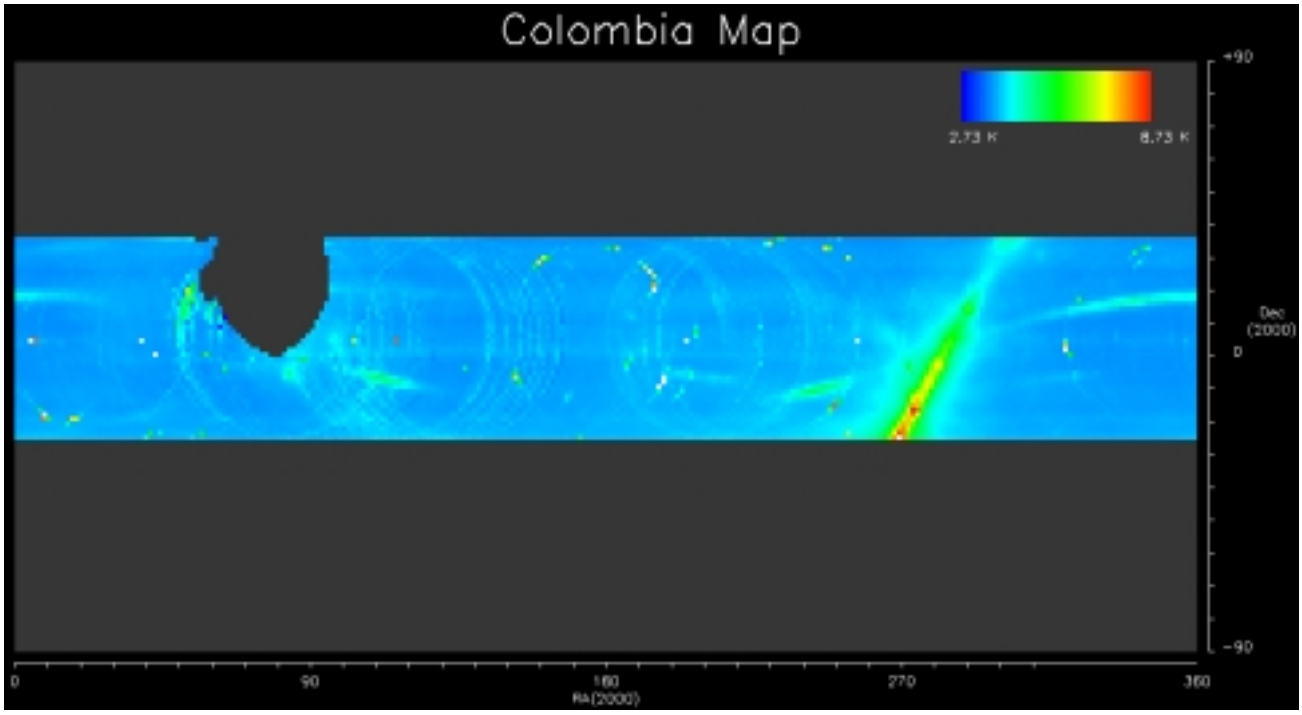

(b)

Figure 13: (a) Raw Brazil data with artificial baseline. (b) Raw Colombia data with artificial baseline.

3°. GEM maps at 2.3 GHz are made at 1.4° pixel size, covering the entire sky by 256 x 128 pixels. Figure 13 shows the preliminary Brazil and Colombia maps.

4.4.4 RFI Removal

As it can be seen from the maps, there is severe RFI contamination in both Brazil and Colombia data. Some of the sources of these RFI are known. For example, the two bright spots on the northern declinations of the Brazil map are due to a cellular telephone tower in the town of Cachoeira Paulista which is towards the North of the dish location. As it can be seen, maybe except the sun, they are the brightest objects on the sky (although due to the saturation point of the apparatus they are essentially the same, see azimuth offset section). However, it is relatively simple to eliminate most of the signal due to the tower. In time ordered data, it is easy to distinguish the peaks corresponding to the tower. Since the tower is localized in azimuth, a simple azimuth cut at the binning stage rejects most of the signal due to the tower. We were lucky in the sense that this azimuth cut happened to be between 190° and 210°. If it had extended to 180°, this procedure would have resulted in declination band loss since the northern and southern most declination pixels are averaged from one azimuth while all the other declinations are collection of signal from to azimuths symmetric around 180°. Figure 14a is the result of the stationary RFI beacon removal.

In addition to the RFI beacons, there seems to be random RFI contamination in the Brazil map. The source(s) of this contamination is not exactly known, although there is speculation that it may be due to a microwave oven used in the observation room. The identification of these bright spots on the map as RFI depends on the fact that all the hits for these pixels are somewhere between 4 and 10 K except for one hit which happens to be around 300 to 400 K. Also, since these peaks are isolated in time ordered data, it is safe to assume that they are not the galactic signal. They are removed by a 3 σ cut criterion where all the hits in a given pixel 3 standard deviations above and below the mean are rejected. The map is filtered twice to eliminate any biasing in the calculation of the mean and the standard deviation due to the large spikes. Figure 14b shows this filtering on the map in 14a.

There is no apparent RFI beacon in the Colombia data. However, we do see some random RFI signatures similar to the Brazil map. These are checked and removed using the same method. A much more interesting and somewhat mysterious source of RFI is the sinusoidal striping. The fact that it seems to follow an ecliptic-like

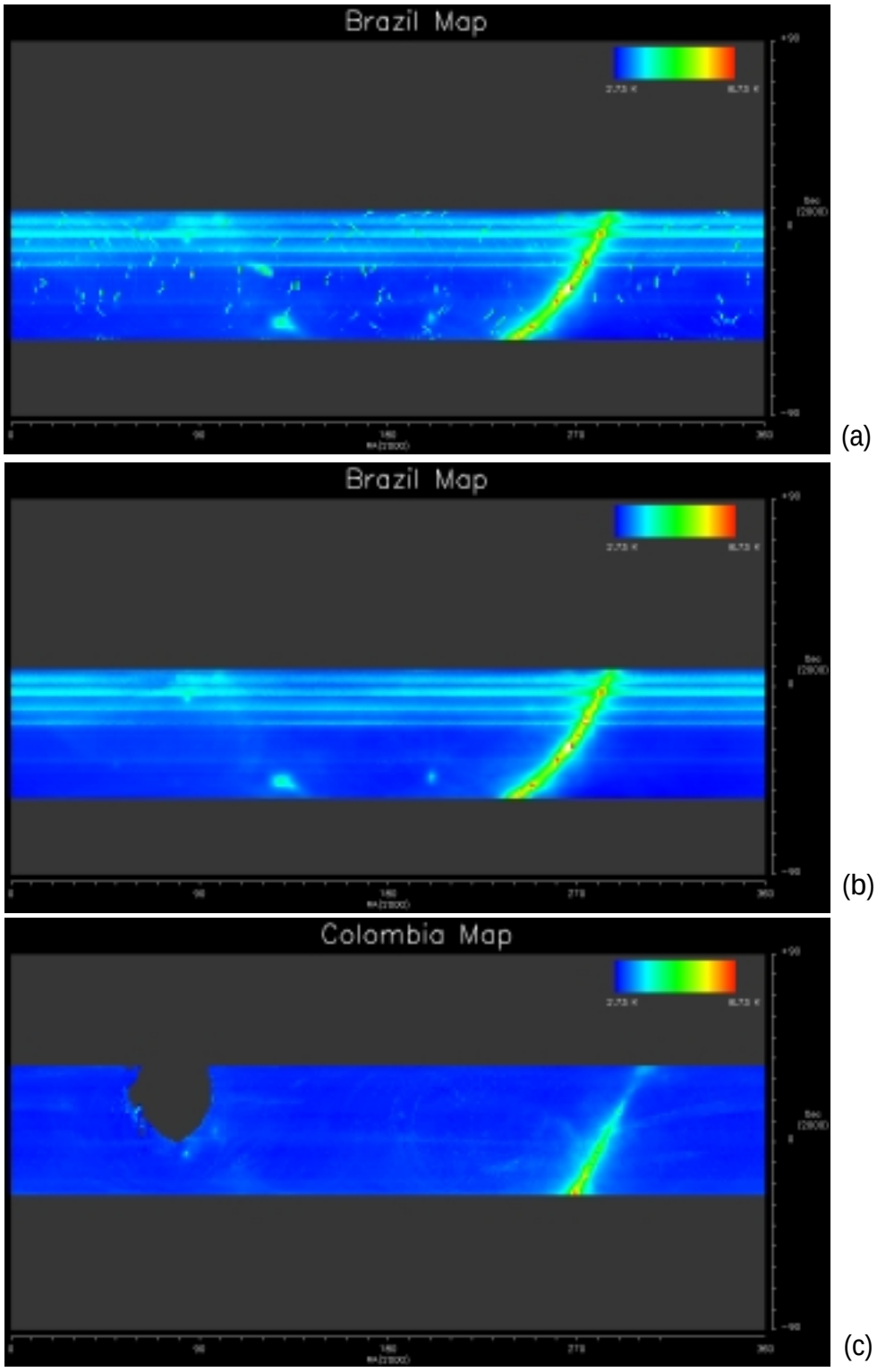

Figure 14: (a) Azimuth cut between 190° and 210°. (b) 3 σ filtering on the same map (c) 3 σ filtering and structured RFI removal on Colombia map.

path suggests the possibility of a satellite in orbit. The most interesting feature of this signal, however, is that the hits in the pixels contained in the striped regions are correlated with the azimuth the hits came from. As a result, the mean of the hits from the East is higher than the mean of the hits from the West. This fact was used to eliminate the striping. However, as it can be seen in figure 14c, this procedure was not entirely successful.

4.4.5 Ground Striping Removal

The last part of the RFI removal for Brazil involves removing contamination from the ground through the sidelobes. This contamination coupled with the observational technique results in striping in the scanning direction. To remove the striping, a template is needed for the contamination. We will make several assumptions about the nature of the source: the contamination is only azimuth dependent, and the intensity does not change with time. These assumptions are most likely unphysical but seem to work well for at least a first order approximation. Therefore, we model the signal received as:

$$Signal(i,j) = S_{sky}(i,j) + G(\phi(i,j)) + N(i,j) \tag{16}$$

where S_{sky} is the signal from the sky; G is the azimuth dependent stationary ground signal; and N is the gaussian noise associated with the measurement.

We use an iterative method suggested by Dr. Smoot to destripe the map. Before I describe the method, some definitions are necessary to clarify the procedure. In the following equations, $\mathcal{S}$ will denote the raw pixelized data that has been twice 3 σ RFI removed. $\mathcal{S}$ is a three dimensional object where the two dimensions denote right ascension and declination, while the third dimension contains the hits for the given pixel. $\mathcal{M}(i)$ will denote the resultant stripe-removed map at the ith iteration. $\mathcal{G}(i)$ will denote the stationary template to be subtracted on the (i+1)th iteration. The process begins with the construction of $\mathcal{G}(0)$ from $\mathcal{S}$ as follows:

$$\mathcal{G}(0) = < \mathcal{S} >_{azi} \tag{17}$$

We essentially bin all the data by 0.5° bins and average over the bins to come up with a value to subtract from the raw data depending on its azimuth (see figure 15). $\mathcal{M}(1)$ ($\mathcal{M}(0)$ is simply $< \mathcal{S} >_{pix}$) is the result of this subtraction. More precisely,

$$\mathcal{M}(1) = < \mathcal{S} - \mathcal{G}(0) >_{pix} \tag{18}$$

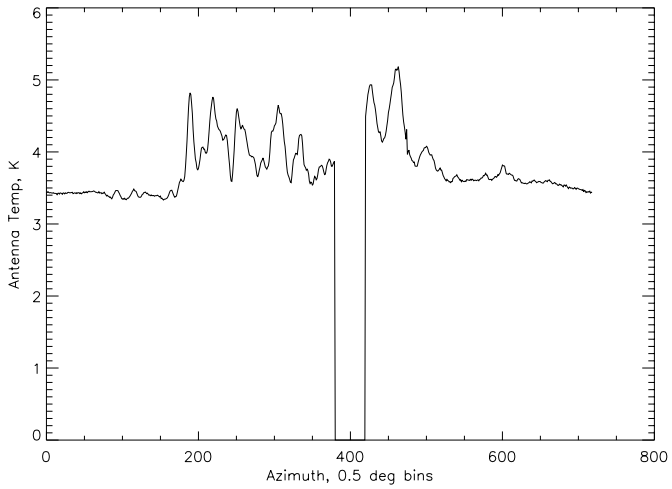

Figure 15: The initial ground profile in Brazil. The large gap in the middle is due to the azimuth cut.

where $< .. >_{pix}$ denotes usual averaging of a pixel. As a result $\mathcal{M}$ is a two dimensional ra/dec map. The process would be complete at this point, if $\mathcal{G}(0)$ had been the correct template. From the definition of $\mathcal{G}(0)$ in 17, we see that the template also includes real features from the sky such as the galactic plane. These real features are either concentrated on a specific azimuth range or their temperature is not constant over the entire azimuth range (such as the galactic plane). As a result, their contribution to the template must be removed iteratively. So, we construct the new template as follows:

$$\mathcal{G}(1) =< \mathcal{S} - \mathcal{M}(1) >_{azi} \tag{19}$$

By averaging the difference between the raw data and the 1st order corrected map, we begin to force the real features in the template to zero. The process continues until the difference between templates becomes smaller than some desired value.

In practice, we noticed that the first iteration results in a drastic improvement in the map (compare figure 16 to 14b). Successive iterations, result in very small changes that are insignificant from a visual point of view but are necessary to improve the accuracy of the process. Figures 16 and 17 summarize the process and the resultant maps.

There are couple of more details that are worth mentioning at this point. For reasons we cannot determine, the procedure fails for the southern most declination band. With every iteration, the new ground profile is forced towards zero for the

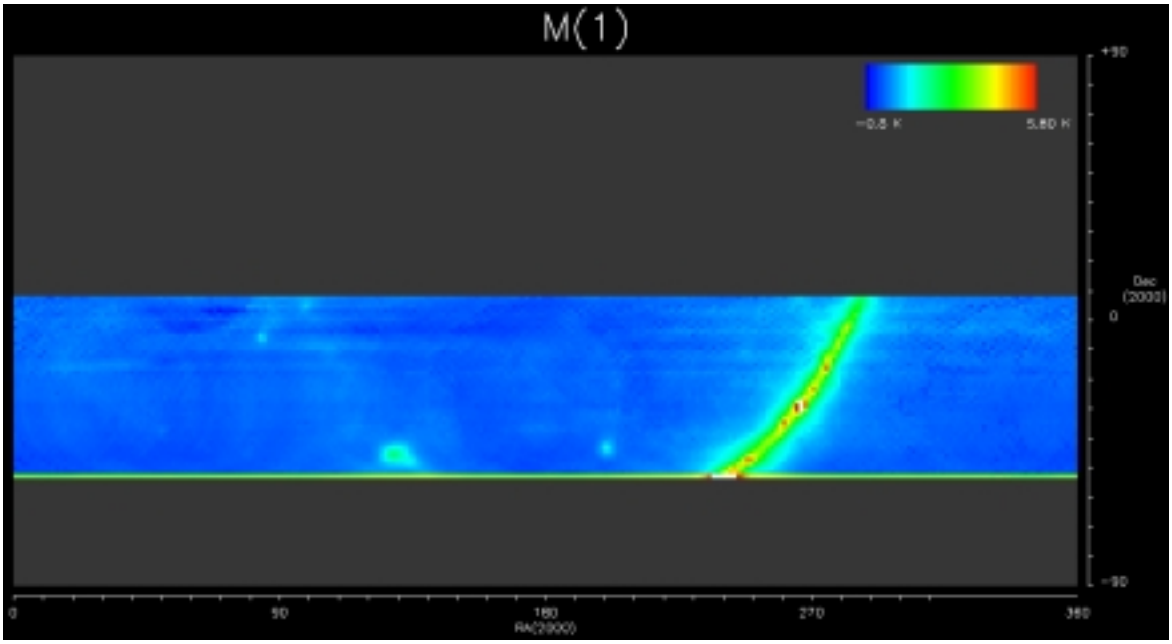

(a)

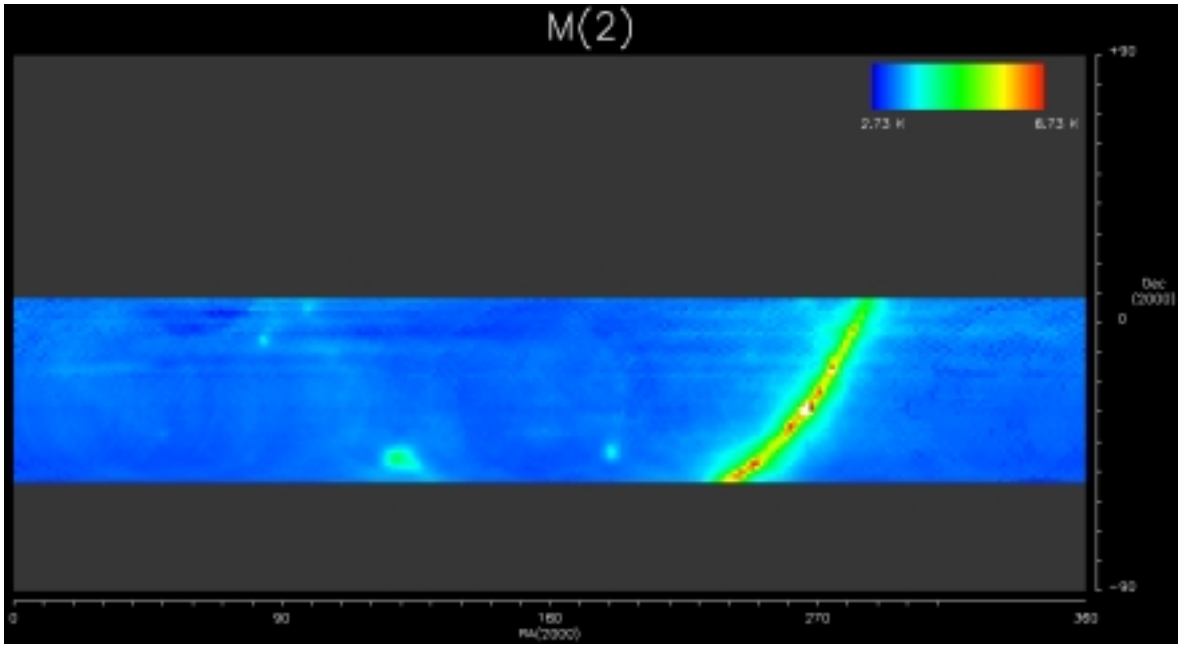

(b)

Figure 16: (a) The first clean map. The southern most declination band is not included in the process, and as a result it does not shift with rest of the map. (b) The second itteration result. The entire map has been shited up to the original temperature range using the cold region.

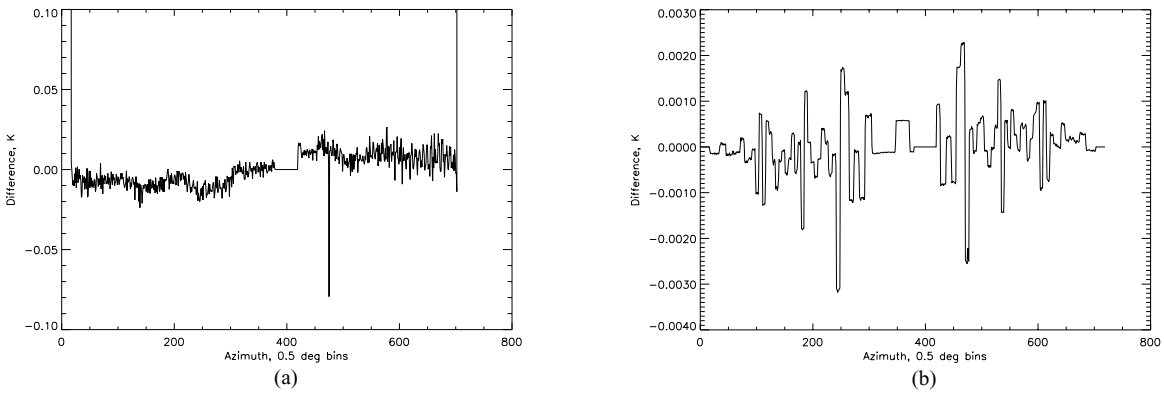

Figure 17: (a) Difference between 1st and 2nd ground profile. (b) Difference between 2nd and 3rd profile.

azimuths corresponding to this declination band. As a result, the de-striping algorithm was not applied to the southern most declination band. We suspect that this problem is due to either the increased azimuth range for this pixel[1], or the fact that the azimuth values are continous for this declination band while there are two distinct values for the rest. The other problem is that due to the nature of the process, the average values of the pixels are forced negative since we are subtracting means from hits. As a result, we need a procedure to bring maps back up to the correct temperature range. This is accomplished by keeping track of temperature of a cold region in the map that is far away from striping. The region used, -34° $< \delta <$-22°, 36° <RA<60°, is identified as a quiet region of the sky by Banday. This region also happens to be stripe-free.

4.5 Receiver Calibration

Now that we have developed the necessary RFI removal procedure, we are in position to go back and determine system parameters. The procedure outlined below was applied only to Brazil data due to several problems in Colombia. As discussed earlier, the feed horn is out of focus in Colombia, making it quite difficult to predict the exact beam pattern. Moreover, due to electrical problems that shift the baseline of the data from negative to positive in few frames even though the data is stable for hours on

[1]Due to the scanning pattern, the data bunches up towards the northern and the southern most pixels. The reason why this effect is not seen in the north is that the northern most declination band is only half-filled with data.

each side of the ramp, it is impossible to rely on Colombia data without the artificial baseline which renders parameter calculations useless.

4.5.1 Gain

In order to determine the gain of the system, we must compare the antenna temperature of a physical source at a known temperature with the voltage recorded for that object. Again, the moon and the sun are the basic sources that are used in the calibration. However, in order to determine the antenna temperature of these sources, the beam pattern of the dish-horn assembly must be known. Since the beam pattern of the apparatus was not determined prior to observations, we will deduce it from the data. In order to achieve this, we go back to the data before any of the mapmaking and RFI removal procedures. At that point, the signal is still in volts and in time order with no baseline corrections. Using the ephemeris generated in the shaft encoder calibration, the two orthogonal angles between the source and the beam are calculated. The result is put in a 2 dimensional array with the center of the array corresponding to the beam right on top of the source. Figure 18a and b are the results of this procedure for the moon and the sun. Since the sun is so hot, the temperature as it approaches the beam becomes greater than the maximum voltage allowed by the DAS and also probably saturates the amplifiers. As a result, the center portion of the beam pattern does not exist for the sun. Similarly, since the moon is not too strong of a source, the beam pattern drops below the noise floor very quickly, and hence the tails of main lobe and the side lobes are not visible.

These limitations coupled with the fact that we have projected a beam pattern on a sphere on to the plane lead to problems in least-square fits to the beams. The initial approach was to fit two dimensional gaussians to the beams using IDL's native "gauss2dfit" program. Several limitations with the program such as inability to enter errors associated with each point, and the programs need for a peak value given in the data prompted a new version of this program, written by James Lamb. However, due to uncertainties with the fit parameters resulting from limitations discussed above and uncertainty in the temperature of the sun which depends on the sun spot cycle,it was impossible to determine the parameters from the sun in Brazil. As a result, we wanted to try something a little more complex. A closer inspection of the sun beam pattern reveals a ring around the main lobe. This is to be expected since the beam

pattern for a circular aperture is given by:

$$I(\theta) = I_0 \left(\frac{J_1(krsin\theta)}{krsin\theta} \right)^2 \tag{20}$$

where k=$2\pi/\lambda$, r is the radius of the aperture and J_1 is the first Bessel function of the first kind. Starting from this point and allowing for different widths in the two orthogonal directions I wrote a new curve fitting program that fits data to:

$$I(\theta,\phi) = A_0 + I_0 \left(\frac{J_1(ksin(\sqrt{\left(\frac{\theta - s_\theta}{a}\right)^2 + \left(\frac{\phi - s_\phi}{b}\right)^2}))}{ksin(\sqrt{\left(\frac{\theta - s_\theta}{a}\right)^2 + \left(\frac{\phi - s_\phi}{b}\right)^2})} \right)^2 \tag{21}$$

where A_0 is the DC constant to compensate for the noise floor, s_θ and s_ϕ are the offsets from the center in radians, and a and b are the parameters associated with the FWHM by:

$$\theta_{FWHM} = a(sin^{-1}(2 * 3.832/k)) \tag{22}$$

$$\phi_{FWHM} = b(sin^{-1}(2 * 3.832/k)) \tag{23}$$

Unfortunately, this fitting program is really sensitive to the initial guesses of s_θ and s_ϕ. Since we did not have the center of the sun beam pattern and due to some noise between the first and second maxima, we could not get the fit to converge on the Brazil sun. As a result, we had to resort to using the moon for the calibration. To calculate the gain, we need to find the antenna temperature of the moon. In general, the antenna temperature is given by [12] [19]:

$$T_A = \frac{\epsilon_r}{\Omega_b} \int_{\Omega_s} T_{source}(\theta,\phi) P_n(\theta,\phi) d\Omega \tag{24}$$

where ϵ_r is the fractional power transmission of the antenna which is close to unity; Ω_s is the solid angle subtended by the source; Ω_b is the solid angle of the beam; and $P_n(\theta,\phi)$ is the normalized beam pattern. We can model the moon as a constant source of average angular diameter 31.12'. At 2.3 GHz, the temperature of the moon is 225 K (see [13]). Therefore,

$$T_{A_{moon}} = \frac{225}{\Omega_b} \int_{-31.13/120}^{31.12/120} P_n(\theta,\phi) d\Omega \tag{25}$$

With the calculated fit parameters (see caption of 18a), the antenna temperature of the moon is 5.749 K. Since the height of the gaussian is 0.1196 V, this results in a gain[2] (G=T_A/V) of 48.07 K/V with a fractional error of 10% propagated through the equations.

[2]Actually, this the inverse of gain. See section on susceptibility for details.

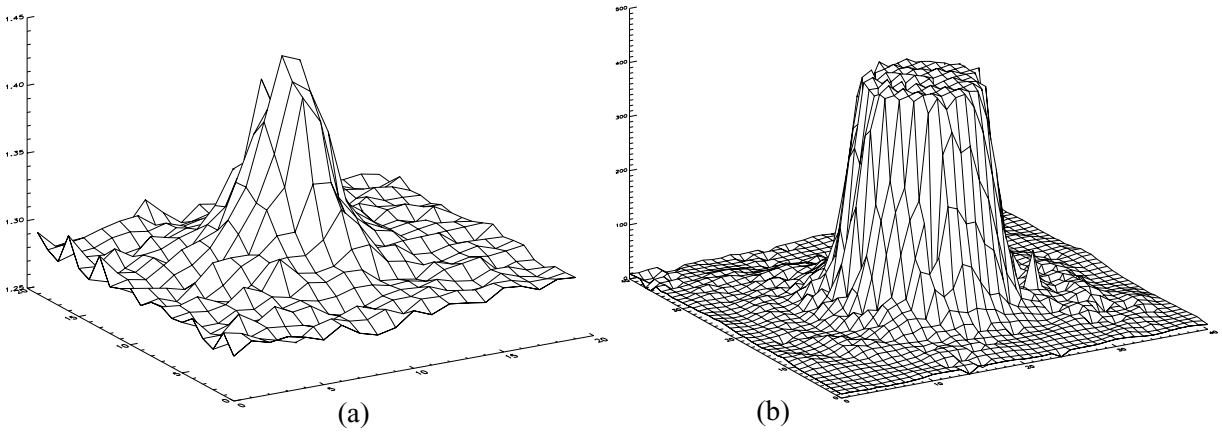

Figure 18: (a) 10° by 10°, 0.5° resolution moon beam pattern (Brazil). Fit parameters are: Noise floor: 1.289 V; peak from noise floor: 0.1196 V; x-width: 2.46°; y-width: 2.92° (b) The beam pattern of the sun in Brazil at 0.5° resolution

4.5.2 System Temperature

System temperature is the inherent noise within the system, and by definition, the temperature the system will detect when the antenna temperature is zero. To determine this value, the standard "Y-factor" method was used [12], [19]. In this method, two sources with known effective temperatures are used to determine the system temperature. The idea is to plot the observed antenna temperature versus the effective antenna temperature of the source and to find the y-intercept of the line connecting the two. To be more precise, we are fitting a line to T_{source}=T_1 scaled by the beam pattern (for the moon, this is 5.749 K quoted above plus the factor $2.73(\Omega_b - \Omega_s)/(\Omega_b)$ to take into account the background surrounding the moon) versus observed volts (T_1+T_{sys} in volts). As a result, T_{sys} is given by:

$$T_{sys} = \frac{T_1 - YT_2}{Y - 1} \tag{26}$$

where

$$Y = \frac{T_1 + T_{sys}}{T_2 + T_{sys}} \tag{27}$$

Since we were not able to determine the antenna temperature of the sun, we were forced to find another source to use as the cold load. The cold region discussed in ground removal was used as the cold load. The assumption made was that in this region, the temperature of the sky is equal to the CMB temperature of 2.73

K (since we are well within the Rayleigh-Jeans limit of the Blackbody curve the ν^2 dependence is canceled out by the ν^{-2} scaling of the intensity by the receiver). As a result, the system temperature includes not only the receiver temperature but also the temperature due to atmosphere, ground etc. (excluding CMB). Finally, the value of the system temperature was determined to be 57.37 K with a $\sim$ 10% fractional error due to uncertanties in the moon temperature (gaussian fit).

4.5.3 Susceptibility of Gain to Temperature

The last system parameter that must be determined is the susceptibility of the gain to the physical temperature of the receiver. To simplify analysis, we will restrict this temperature dependence only to the first stage amplifier and determine its susceptibility. Once again, to determine this parameter, we make use of the cold region in the Brazil map. Figure 19 is a plot of the antenna temperature versus the physical amplifier temperature. As it can be seen, the dependence is quite linear with a negative slope. The least square fit to the data results in a susceptibility, ξ, of -0.022 $\pm$ 0.0026 V/K.

These three parameters are used in the following way to determine the conversion factor between the signal in volts and the signal in Kelvin. First of all, the parameter we called gain above is not actually the gain but the inverse of the gain. Notice that we have some input power, which by the use of a detector diode is converted into an output of volts. As a result, we have:

$$Volts = G * T_A \tag{28}$$

Therefore, the conversion factor we want is G^{-1}. However, for the calculation I will work with G and at the end find G^{-1}. The gain of the system is divided into two parts to model the temperature dependence of it in the simplest way as follows:

$$G = G_0 + \Delta G(T_{amp}) \tag{29}$$

where G_0 is the constant component of the gain that was calculated above. In general, we can determine ΔG from:

$$\Delta sig = \Delta G * T_{sys} + G * \Delta T_{sys} \tag{30}$$

However, the effects of these two terms compete against each other since the gain goes down with increasing temperature and the system temperature goes up. Since

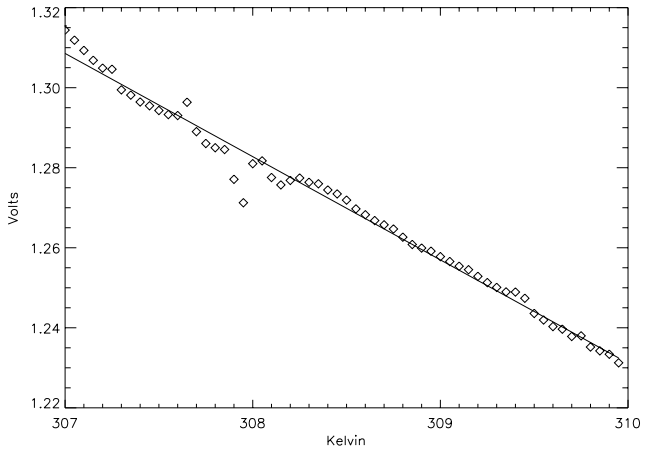

Figure 19: Antenna Voltage vs HEMT temperature in the cold region defined by Banday.

the slope in Figure 19 is negative, the first term is the dominant factor, and therefore, we will neglect the second term. Then, Δ G can be written as:

$$\Delta G = \frac{\Delta sig}{T_{sys}} = \frac{\xi \Delta T}{T_{sys}} \tag{31}$$

where ΔT is the difference between a reference temperature and the temperature of the amplifier for the given frame. A natural choice for the reference temperature is the mean amplifier temperature of all the hits that make up the beam pattern of the moon, since the constant component of the gain was calculated using it. Finally, the conversion factor, G' is:

$$G' = \frac{1}{G_0 + \Delta G} = \frac{1/G_0}{1 + \frac{\Delta G}{G_0}} = \frac{G'_0}{1 + G'_0 \Delta G} = \frac{G'_0}{1 + \frac{G'_0 \xi \Delta T}{T_{sys}}} \tag{32}$$

where G_0' is the value calculated in the Gain section.

Once these parameters were determined, they were used to create a new moon beam pattern in antenna temperature rather than in volts. A new estimate of the G_0' was calculated to be 53 V/K which is within the error allowed by the first calculation. A new system temperature was also determined. To rule out systematic increase in the gain, a new moon beam pattern was made using the new parameters which resulted in 45.2 V/K which is also within the error of the original value. Since, the values oscillate about the original value, we decided to use the value calculated in the gain section. Figure 20a and b are the comparison of the Brazil map with incorrect (initial guess) and correct system parameters. The artificial baseline is not applied

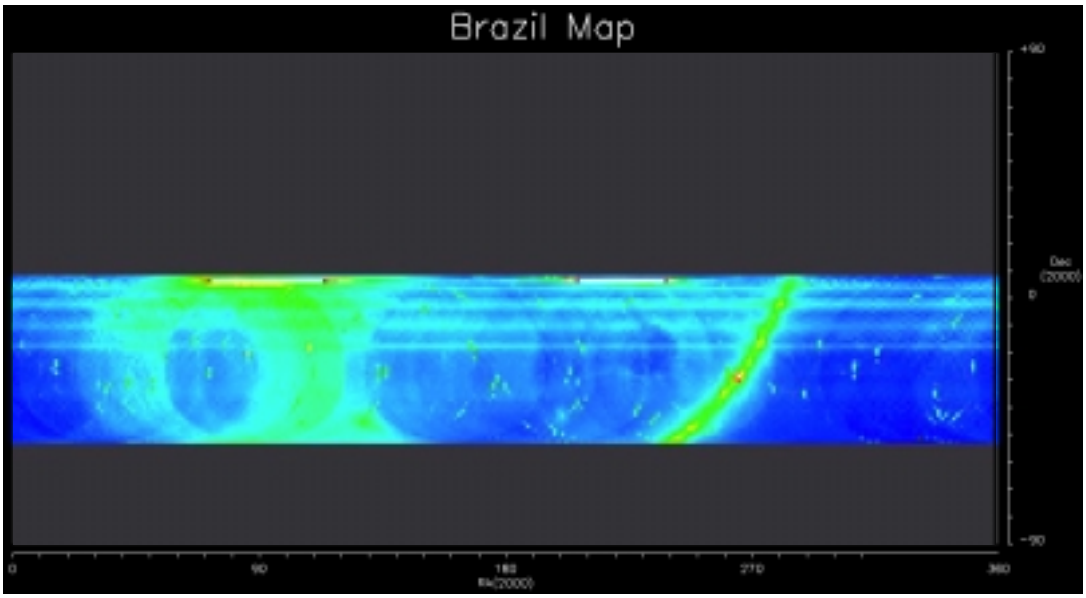

(a)

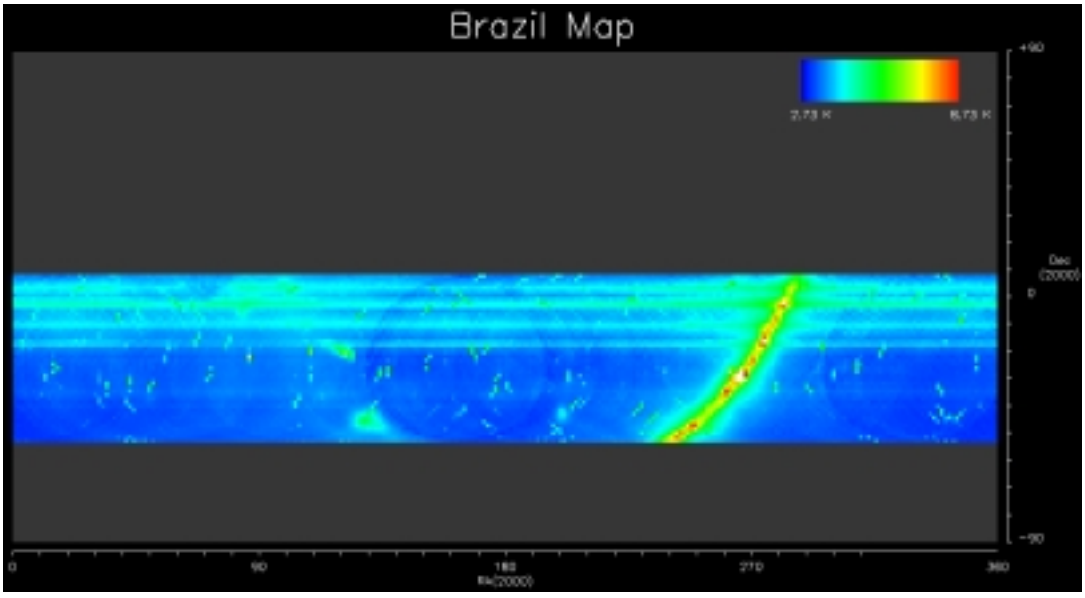

(b)

Figure 20: (a) Brazil map with incorrect susceptibility and without artificial baseline. (b) Brazil map with the calculated susceptibility, also without baseline

to reveal the effect of susceptibility. The low RA region in 20a where the signal is high is due to the sun. Although the amplifier gain goes down with the increasing amplifier temperature, the incorrect value of the susceptibility over-corrects for the decrease in gain, resulting in a higher gain than necessary. Figure 20b shows that this over-correction is much less with the new values but not entirely gone. Therefore, a more comprehensive calculation of the susceptibility is needed.

4.6 Map Merging

As discussed above, the system parameters could not be calculated reliably for the Colombia data. Since an overlap between the two maps exists, we decided to calibrate the Colombia map using the Brazil map. The Colombia data is converted into a ra-dec map without any conversions of the signal, resulting in a voltage map. The artificial baseline is used to correct the baseline drifts. Once the map is made, the standard RFI removal procedures are applied. The Brazil data is binned using the system parameters, RFI cleaned, and ground stripping removed (2 versions were made: one with the artificial baseline and one without).

We decided to use the declination band $\sim 65° < \delta < 70°$ for the calibration since the two maps overlap and the Brazil map does not have any striping in this region. The mean temperature in each pixel within these declinations was written into an array for both of the maps, and a least square fit was fit to the following linear equation:

$$Signal_{Brazil,K} = G' * Signal_{Col,V} + T_{sys} \tag{33}$$

Of course T_{sys} in this equation does not correspond to any physical system temperature since the artificial baseline minimum is arbitrary and because the system temperature is already subtracted from the Brazil data. The calculated values for G' and T_{sys} are 45.3 K/V, -6.6 K and 44.1 K/V, -9.1 K. The first set is for the Brazil data that was not corrected with the artificial baseline, and the second one is for the Brazil data corrected with the artificial baseline. The calculated G' are within the error of the G' calculated for Brazil data.

Once the calibration parameters are determined, the maps are merged simply by combining the hits for each pixel from both of the maps. Figure 22 and 23 are the final results of the data analysis. Initially, we had hoped that the merging of the two maps would result in a further reduction of ground removal in the striped region. Unfortunately, due to the differences in the length of observations, the Brazil data

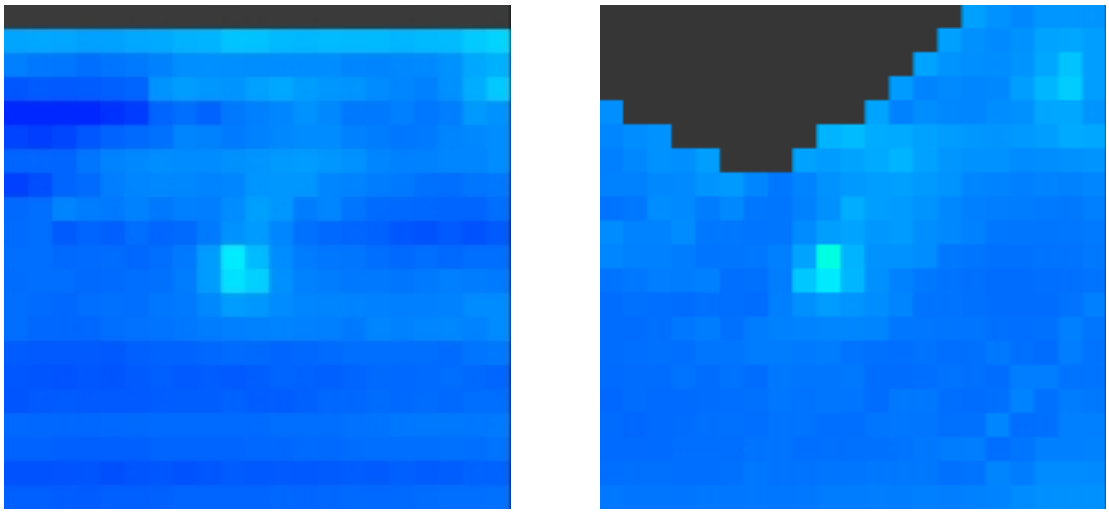

Figure 21: (a) and (b) are the same exact region from Brazil and Colombia map. Since the bright spot is on the same pixel, the pointing is correct on the maps.

dominates in the overlap region. At first glance, it seems as if there is a pointing difference between the two maps, especially due to the way galaxy looks at the seam. This is not due to the pointing but a result of the ground striping still present in the Brazil data (see Figure 21).

A total of 542.9 hours of data taken in Brazil and 159.3 hours of data taken in Colombia was used. In Brazil data, 40.7 hours of data was removed due to noise source firings; 28 hours of data was removed due to stationary RFI beacon; 13.9 hours of data was removed due to 3 σ filtering; 11.7 hours of data was removed due to sun and moon cuts. Overall, 17.4% of the data was rejected. In Colombia data, 11.95 hours of data was removed due to noise source firings; 26.5 hours of data was removed due to structured RFI; 3.6 hours of data was removed due to 3 σ filtering; 13.4 hours of data was removed due to sun and moon cuts. The overall percentage of data rejected was 34.8%.

5 Conclusion

Although there is a major improvement between the initial and the final maps, there is definitely room for more. In this last section, I would like to summarize a few new

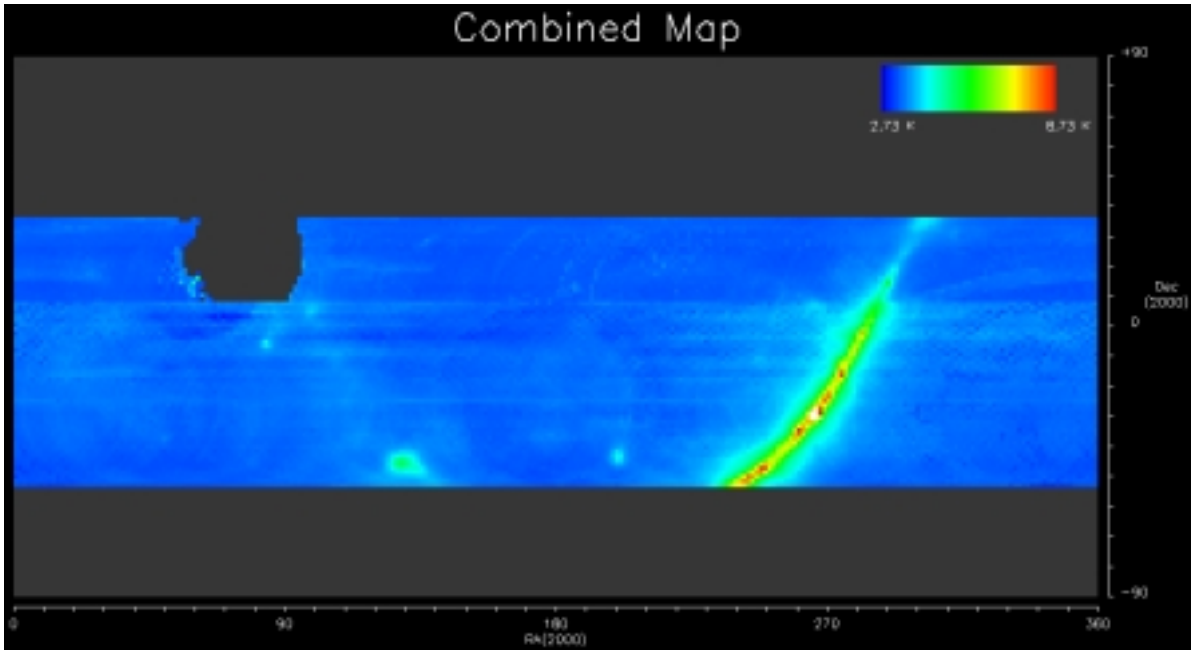

Figure 22: Combined map. Brazi map has no artificial baseline correction.

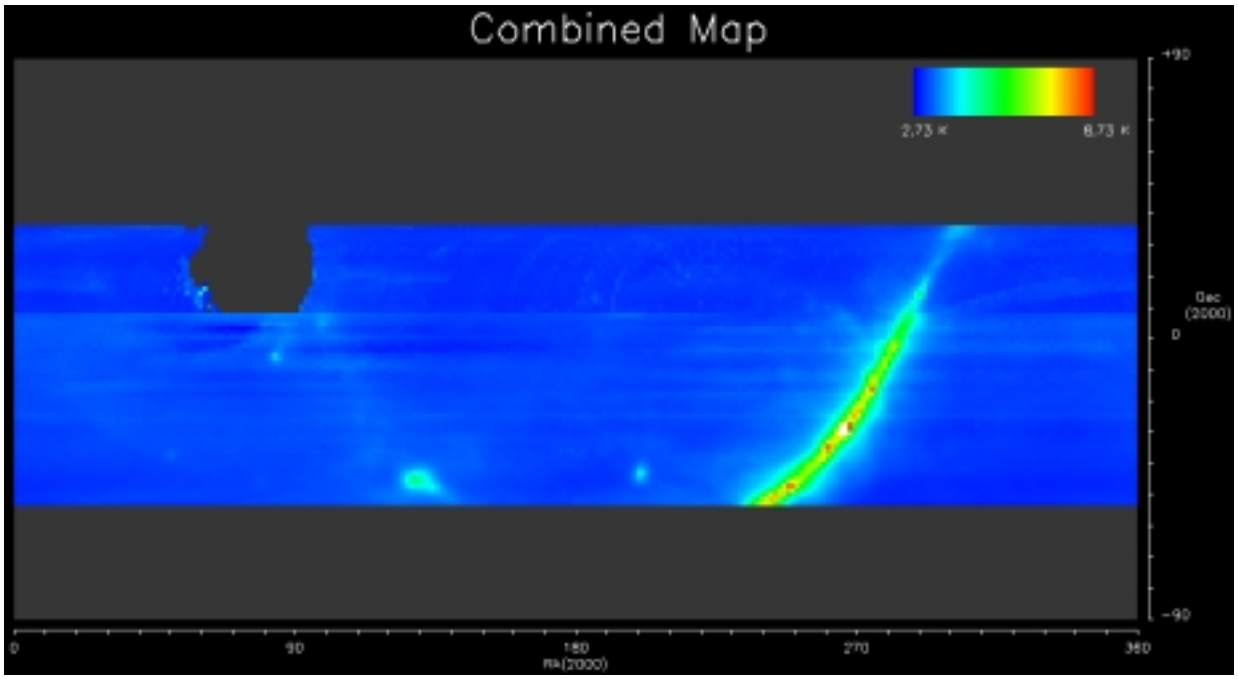

Figure 23: Combined map. Brazil map has been corrected using artificial baseline. Although not a desirable solution, it suggests that other baseline correction methods must be pursued in the future.

experimental observations and analysis techniques that could be implemented in the future.

Baseline Figure 23 shows the room for improvement for the map in 22. However, the current procedure used in the artificial baseline is not favorable due to the flattening of the spatial spectral index variation. A different way of correcting the baseline without removing the spectral index information is given in Tello [22] and Delabrouille [6]. The scanning pattern can be exploited to network rotation circles in the sky, and calibrate rotations that intercept each other. Since most of the 1/f noise below the rotation period can be averaged out, time order data can be averaged for ~ 5.64 minutes (the time it takes for the Earth to rotate from one pixel to the next in RA for 1.41° pixels). Delabrouille shows that the remaining low frequency noise creates offsets for different circles. A least-square method can be implemented to minimize all the offsets of all the circles intersecting the reference circle simultaneously. Then, the baseline can be propagated across the entire declination band by using the last calibrated circle.

Another approach is to examine the noise source firings with a little bit more care. Although they seemed unreliable on the first glance, there may be parts of the noise source firings that may be useful in correcting in the baseline. Since a new noise source is being purchased (the old one eventually stopped working completely), it can definitely be a factor in baseline correction for data taken in the future.

Ground Striping The current data from Brazil shows that the ground shield in place at the moment is not adequate for 2.3 or higher frequencies. Plans are being made at the moment to replace the fence with a solid aliminum sheet with 7mm holes in it. The new ground shield should improve the ground contamination drastically at 2.3 GHz. However, this should be verified at the early stages of the observation period to avoid lengthy data analysis later on as is the case for the current data. In addition to the improvement in the shielding, observations at different zenith angles will also help in the data analysis phase. Data from multiple zenith angles will couple additional azimuth angles with any given declination band or any given azimuth angle with multiple declination bands leading to more robust de-striping algorithms.

System Parameters It would be quite helpful if system calibration was attempted at the observation phase rather than the data analysis phase. Granted that a hot-cold load test of the entire apparatus would be quite difficult, at least a hot-cold load test for the receiver should not be too difficult to implement. The receiver, due to its small size, can easily be inverted onto a liquid nitrogen tub or covered with anechoic material at room temperature for this test.

In terms of the beam pattern, the antenna test range of the Integration and Tests Laboratory at INPE (the Brazilian National Institute of Space Research) can be used at least to get a beam pattern of the feed horn. In addition, special data sets dedicated just to moon scans can decrease the uncertainties in the beam pattern construction in the data analysis phase. Relatively rapid rotation speed of the dish ($\sim 3^\circ$ are integrated into one frame) leads to the stretching of the beam pattern along the scan direction. After the pointing has been determined reasonably well (again, this would require data analysis to begin as the data is being taken), the dish can be stopped at the azimuth of the moon at the elevation of the beam and let the moon slowly rise to the beam elevation.

References

[1] Banday, A. *Fluctuations in the Cosmic Microwave Background*, Ph.D. Thesis, 1992

[2] Bastian, T., et al. 1996, *Astrophys. J.*,, **473**, 539

[3] Bennet et al. 1992, *ApJ.*, **391**, 474

[4] Buhl D. and Tlamicha A. 1968,*Astrophys. J.*, **153**, L189

[5] Christiansen W. and Högbom, *Radiotelescopes*, Cambridge University Press, 1969

[6] Delabrouille J. 1997, *Astron. Astrophys. Suppl. Ser.*, **127**

[7] De Zotti G. et al., 1999, *American Institue of Physics* , **476**, 204

[8] Haslam et al., 1982, *A&AS*, **47**, 1

[9] Heafner, *Fundamental Ephemeris Computations*, William-Bell Inc., 1999

[10] Keihm, S., 1979, *LPI*, **10**, 649

[11] Kheim S., 1983, *ICARUS*, **60**, 567

[12] Krauss J., *Radio Astronomy*, McGraw-Hill Book Company, 1966

[13] Krotikov V. and Pelyushenko S. 1985, *Soviet Astronomy*, **31**, 216

[14] Linsky J., 1973, *Astrophys. J.*, **25**, 163

[15] Lo Y. and Lee S., *Antenna Handbook*, Vol. 2 Van Norstrand Reinhold, 1993

[16] Lyons L., *Data Analysis for Physical Science Students*, Cambridge University Press, 1991

[17] Manly B., *Multivariate Statistical Methods*, Chapman and Hall, 1994

[18] Marsh K. and Hurford G., 1982, *ARA&A*, **20**, 497

[19] O'Neil K. 2001, *ASP Conference Series*

[20] Platania P. et al., 1998 *Astrophys. J.*, **505**, 473

[21] Reich and Reich, 1988, *A&AS*, **174**, 7

[22] Tello C. et al., 2000, *ASP Conference Series Vol. IAU Symposium 201*

[23] Tello C. et al., 2000, *A&AS*, **145**, 495

[24] Torres S. et al., 1996, *A&AS*, **240**, 225

[25] Torres S. and Smoot G., 1997, Internal Paper

[26] Troitsky A., 1962, *IAUS*, **14**, 475

[27] Woan G., *The Cambridge Handbook of Physics Formulas*, Cambridge University Press, 2000

[28] Zirin H. et al., 1990, *Astrophys. J.*, **370**, 779